ADVANCED GUIDANCE ALGORITHMS

FOR THE

ARES V CARGO LAUNCH VEHICLE

A Thesis

presented to

the Faculty of the Graduate School

at the University of Missouri-Columbia

In Partial Fulfillment

of the Requirements for the Degree

Master of Science

---

by

SHELLY SU

Dr. Craig Kluever, Thesis Supervisor

AUGUST 2008

ACKNOWLEDGEMENTS

I would first like to thank my advisor Dr. Craig Kluever for all his guidance through both the generation and presentation of the material contained in this thesis. His supervision has kept my research both focused and productive, and I greatly appreciate the education I have gained and all opportunities that have come my way under his mentorship. I know that all he has taught me will serve me well in the years to come.

I would also like to express my gratitude to Dr. Greg Dukeman and the rest of the GN&C and Mission Analysis Branch at Marshall Space Flight Center for all their assistance throughout the research process. Thanks to the NASA Graduate Student Researchers Program, Mark Whorton, and the rest of his group at MSFC for supporting this study.

Finally, to all my family and friends, a big thanks for all your support and encouragement.

TABLE OF CONTENTS

LIST OF FIGURES

LIST OF TABLES

LIST OF NOMENCLATURE

Acronyms

AG&C	=	Advanced Guidance and Control
CEV	=	Crew Exploration Vehicle
CLV	=	Crew Launch Vehicle
GN&C	=	Guidance Navigation and Control
IGM	=	Iterative Guidance Mode
MECO	=	Main Engine Cut-off
OTIS	=	Optimal Trajectories by Implicit Simulations
PEG	=	Powered Explicit Guidance
POST	=	Program to Optimize Simulated Trajectories
RLV	=	Reusable Launch Vehicle
FMHR	=	Free Molecular Heat Rate
PLF	=	Payload Fairing

Symbols

A,B	=	steering parameters
a_T	=	thrust acceleration, ft/s^2
c	=	empirical heat-rate constant
g	=	Earth gravitational acceleration, ft/s^2
H	=	Hamiltonian function
h	=	altitude, ft
i	=	angle of inclination, rad
i, j, k	=	coordinate frames
I_{sp}	=	specific impulse of the engine, s
J	=	performance constraint
m	=	vehicle mass, slugs
N	=	interior-point state constraint
q	=	dynamic pressure, lb/ft^2
r	=	vehicle position, ft
t	=	time, s
T	=	thrust magnitude, lbf
u_T	=	unit vector in the thrust direction
V	=	vehicle velociyt, ft/s
α	=	steering angle, rad
β	=	azimuth angle, rad

γ	=	flight path angle, rad
ε	=	Earth flattening rate
θ	=	pitch angle, rad
ι	=	latitude, rad
λ_r	=	position costate
λ_V	=	velocity costate
μ_E	=	Earth gravetational parameter, ft^3/s^2
π	=	analytical jump condition
ρ	=	atmospheric density, $slugs/ft^3$
φ	=	longitude, rad
Ψ	=	terminal state constraint
ω	=	Schuler frequency, rad/s

Subscripts

0	=	initial value
1	=	pertaining to stage 1
2	=	pertaining to stage 2
f	=	final value
go	=	range-to-go value
i	=	vector or quantity relative to the inertial frame
PLF	=	pertaining to point of PLF jettison
ref	=	vector or quantity relative to the reference frame

ADVANCED GUIDANCE ALGORITHMS FOR THE ARES V CARGO LAUNCH VEHICLE

Shelly Su

Dr. Craig A. Kluever, Thesis Supervisor

ABSTRACT

Launch ascent guidance is an area that routinely involves applications of optimization tools and optimal control theory. The vacuum ascent trajectory problem has been formulated as a two-point boundary-value problem with an interior-point state constraint and is solved with a method of direct parameter optimization. The direct method simplifies the more complicated full costate problem and an off-line trajectory optimization routine for the Ares V Cargo Launch Vehicle (CaLV) shows optimal performance as compared to trajectory simulations performed in the industry standard software, Optimal Trajectories by Implicit Simulation (OTIS). The guidance solution may also be determined through an analytic method, developed by assuming polynomial approximations for the steering profiles and flight-path angle profiles. The analytic solutions prove to be useful when applied to the Shuttle-based Powered Explicit Guidance (PEG) routine, where the results have been shown to converge to near a near optimal trajectory.

Chapter 1

Introduction

1.1 A Vision for Space Exploration

In June 2001, NASA, through a program known as the Space Launch Initiative set for itself the goals of significantly increasing the safety and reliability of the second generation of launch vehicles [1]. In following with the Vision for Space Exploration, announced in 2004 by the President's Administration, the Constellation Program will provide the next major step in space exploration, replacing the Space Shuttle in 2010 with a new generation of transportation systems aimed at providing crew and cargo access to the International Space Station (ISS), the Moon, Mars, and beyond [2]. An important component to the development of a next-generation launch system is driven by the Constellation's Ares Project, whose architecture includes the Ares I Crew Launch Vehicle (CLV), the Ares V Cargo Launch Vehicle (CaLV), and the Orion Crew Exploration Vehicle (CEV). The two-stage Ares I is derived from the Shuttle concept, and are comprised of the five-segment reusable solid rocket booster first stage, and the second-stage liquid oxygen/liquid hydrogen rocket system powered by a single J-2X engine [2]. Intended to lift crews and cargo into orbit, it will lift 25 metric tons and be 10 times safer than the Space Shuttle, primarily due to an in-line design and a launch abort system. The heavy-lift version of the CLV, the Ares V CaLV, will support future lunar exploration missions and will also consist of five Shuttle main engines on the core and two five-segment Shuttle-derived solid-propellant rocket boosters. Although primarily designed to carry cargo, the Ares V CaLV can be human-rated to boost the crew exploration vehicle (CEV) into low Earth orbit (LEO) and trans-lunar orbit [3]. The

CLV/CEV combination will be a much anticipated vehicle, since it will replace the retired Space Shuttle fleet and provide a crewed transportation system to Earth orbits and trans-lunar space.

The Constellation Program is driven by the desire to explore space, extending a human presence across the solar system with the intent to carry out a series of human expeditions, aiming for longer lunar occupation, and eventually establishing a permanent base on the Moon. In order to contribute to the goals set forth by the Space Launch Initiative, the Ares Project seeks to maintain cost-effective operations, at minimum risk of loss of crew or mission and high levels of safety and reliability during all stages of flight. Therefore, it is important for launch ascent mission planning to incorporate highly robust guidance and control algorithms.

1.2 Background

Launch ascent guidance is an area that routinely involves applications of optimization tools and optimal control theory. In fact, on-board algorithms for solving the optimal ascent problem have been the foundation of closed-loop ascent guidance for upper stages of launch vehicles since the 1960s.

1.2.1 Guidance Methods

Guidance algorithms for powered aerospace vehicles must compute the time-varying steering commands of the thrust vector so that the vehicle achieves a desired target state (position and velocity). Typically, launch or ascent guidance methods attempt to reach a target orbit with minimum fuel expenditure.

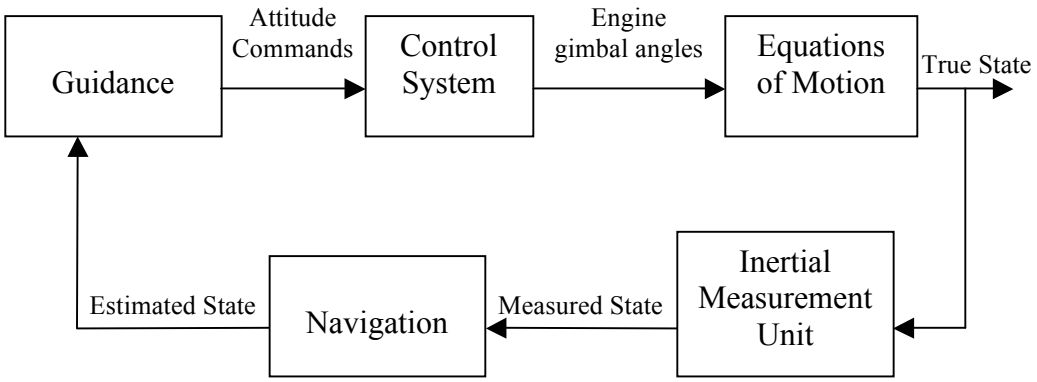

Figure 1.1: General GN&C schematic.

Guidance, Navigation, and Control (GN&C) functions are performed with the use of a flight computer, where the current navigation solution, following Fig. 1.1, is computed using rates from the Inertial Measurement Unit (IMU). For the purposes of this thesis, the estimated and true states are assumed to be equivalent. Guidance then uses the estimated states from Navigation to determine the corrections that must be made to account for the vehicle's current location.

In general, guidance schemes may be divided into two basic philosophies: reference-path methods, and predictor/corrector methods. The first philosophy attempts to guide the vehicle along a pre-planned reference path to the target, illustrated in Fig. 1.2 (a); this technique has been used for entry guidance. By contrast, a predictor/corrector guidance method, seen in Fig. 1.2 (b), re-computes a new path from the vehicle's current state to the target in an iterative fashion, using the current states from the navigation function as the initial condition. Predictor/corrector methods may provide a new path that meets a target condition at a different time than the reference path. By solving the optimal ascent problem in this repeated fashion where the initial condition is updated by the current condition, the guidance solutions are in effect closed loop.

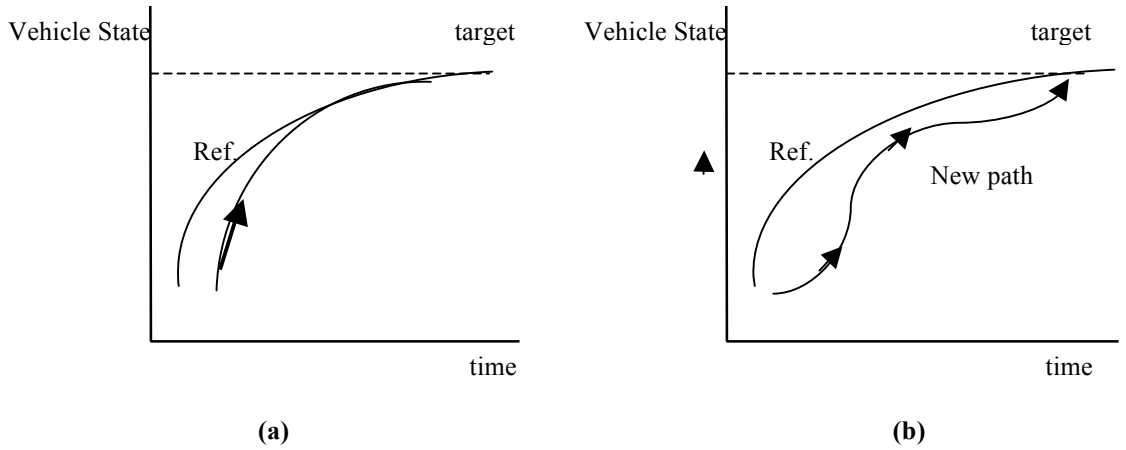

Figure 1.2: Basic guidance philosophies: (a) Reference path method, (b) Predictor/corrector method

Traditionally, predictor/corrector guidance methods have been used for early launch systems. Classical vacuum ascent guidance algorithms based on optimal control theory include the Iterative Guidance Mode (IGM), employed for the Saturn V boosters [4], and the Powered Explicit Guidance (PEG) for the Space Shuttle [5]. In predictor/corrector guidance, the position and velocity at main engine cut-off (MECO) are predicted by using the current values of the states and the estimated thrust-steering parameters. Maneuver target conditions are used to compute the desired position and velocity at MECO. The predicted and desired MECO states are compared, and the differences are used to correct the steering parameters and the updated velocity vector [6]. The predictor/corrector method is then iterated upon until guidance convergence occurs. Hanson [7,8] has recently argued that Advanced Guidance and Control (AG&C) technologies can dramatically reduce the probability of catastrophic failures for launch vehicles as well as reduce reoccurring operational costs. In addition to meeting vehicle safety and reliability requirements, AG&C technologies are critical for reducing expenses involved with guidance and control analysis. References 7 and 8 demonstrate AG&C methods applied to a reusable launch vehicle (RLV) and include simulation test results

for the ascent and entry phases. It is very likely that AG&C concepts will need to be applied to the CLV in order to ensure safety and reliability requirements.

The solution to the optimal ascent trajectory requires the solution to a very complex two-point boundary value problem. Dukeman [9] shows how judicious approximations are made to reduce the order and complexity of the state/costate system, and uses a multiple- shooting method which significantly reduces sensitivity to the guessed initial costates. Recently, Lu et al. have developed a closed-loop ascent guidance scheme for atmospheric flight of an RLV, using the classical finite difference method for the two-point boundary-value problem to produce an on-board solution to the optimal ascent problem [10]. A multiple-shooting formulation, constraint simplification, and a more sophisticated numerical method have enhanced the robustness of an optimal vacuum ascent trajectory algorithm, and is a valuable tool in rapid planning of launch missions [11]. Calise et al. [12] use a hybrid collocation approach in which the optimal vacuum solution serves as the initial guess for the atmospheric flight and aerodynamic terms and path-related constraint terms are gradually introduced using a homotopy method. This method demonstrates reliable convergence and indicates the feasibility of closed-loop endo-atmospheric guidance algorithms.

1.3 Problem Definition

Solving the CLV guidance problem presents many challenges. The presence of interior state constraints complicates the optimal control problem and traditional guidance algorithms do not know about constraints such as heat rate at payload fairing jettison, therefore, the solutions are only sub-optimal. For example, Ref. 13 demonstrates a secant

trajectory optimization procedure combined with a min-*H* steepest-ascent algorithm that produces optimal lifting boost trajectories and displays an efficient convergence speed. Brusch [14] formulates the trajectory optimization problem as a constrained function minimization problem by modeling the control with a function of a finite number of parameters, where the guidance parameters that meet the desired end conditions are determined by assuming a particular form of the steering law that approximates the true optimal solution. Trajectory optimizations of the CLV ascent stage using NASA Langley's Program to Optimize Simulated Trajectories (POST) has shown that significant fuel savings may be realized by "lofting" the trajectory prior to the escape-tower jettison. A simple PEG algorithm applied to the CLV, however, cannot exploit potential fuel-saving maneuvers, as the traditional guidance system is restricted due to its built-in approximations of the dynamics. The motivation for further guidance research, then, becomes to incorporate the capability to treat heat rate constraints into the Ares baseline guidance. These enhancements have potential application for real-time guidance of the Ares launch vehicles, as well as for rapid day-of-launch trajectory optimization.

1.4 Thesis Objective

The objective of this thesis is to develop advanced guidance techniques that improve fuel performance over the current Shuttle-based guidance methods. The algorithm will be based on optimal control theory with interior-state constraints in order to anticipate and compensate for discrete events, i.e. escape-tower jettison and heat-rate constraints. The ascent trajectory optimization problem is formulated such that the control is defined by a function of finite parameters and the control variable is the inertial attitude angle, as

in the IGM formulation for the Saturn V boosters. By using the inertial attitude angle as the control, a nominal trajectory is more easily defined, as the direction of thrust is uncoupled from the path flown [13]. Then, the analytical solutions to the jump condition at payload fairing jettison will be developed, in an attempt to decrease the complexity of the optimization routine.

In addition, this paper will investigate the solutions to the control by developing analytic solutions based on polynomial profiles for the steering angles and flight path angle. Solved in an iterative fashion, the control variables will be updated by iterating on velocity and altitude convergence errors. The converged solutions for the control will be used as an alternative method to provide the initial guess in an on-board, real-time PEG guidance simulation.

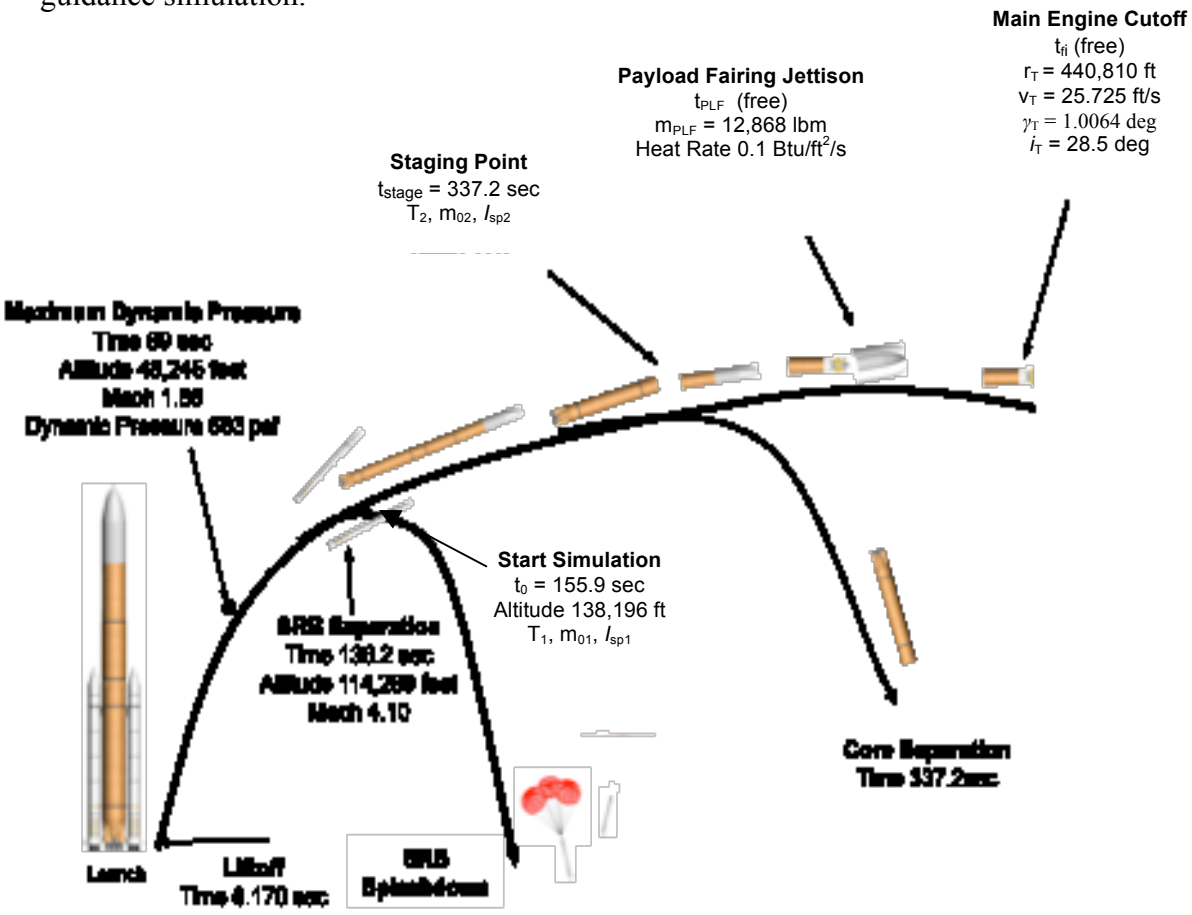

Figure 1.3: Major events from launch to MECO [15].

The Ares V CaLV design concept will be the main test case for this guidance algorithm, but the algorithm should be general enough to be extensible to similar vehicle concepts with different vehicle characteristics. Figure 1.3 depicts the major events for the CaLV from launch to MECO, though for this thesis, only the vacuum portion of ascent flight will be considered. The starting point for simulation has been denoted on the event timeline in Fig. 1.3, where the major events will be the ascent from start time after the initial solid rocket booster (SRB) separation to the MECO target conditions. The ascent flight consists of two burn stages, where the first stage burns for a fixed time and the second stage has a payload fairing (PLF) jettison event at a free (undetermined) time. Trajectory simulations and performance have already been rigorously tested for the Ares V CaLV using the industry standard software, Optimal Trajectories by Implicit Simulations (OTIS), courtesy of the NASA Marshall GN&C and Mission Analysis branch, and will serve as the basis for comparison in this thesis.

1.5 Thesis Overview

The present chapter provides a broad overview of the subject of research for the thesis. Chapter 2 provides a description of the computer simulation environment used to test the guidance algorithm, and Chapter 3 explains the vacuum guidance formulation and necessary conditions for optimal control. Chapter 4 presents in detail the results of the off-line trajectory optimization. Chapter 5 highlights the main features of the PEG guidance formulation and presents an analytical solution method for the vacuum ascent problem. Chapter 6 presents the results of the analytic solution method and the PEG solutions which apply the analytic solutions, and finally, Chapter 7 discusses the merits of the algorithm and provides recommendations for future research.

Chapter 2

Simulation Description

2.1 Overview

In order to evaluate the effectiveness of various guidance algorithms, it is desirable to create computer-based simulations of the vehicle during vacuum ascent. This can be done by numerically integrating the equations of motion to propagate the vehicle's trajectory forward in time. The following sections describe the equations, coordinate frames, and assumptions used in the simulation environment. All simulations were implemented in MATLAB version 6.5.0.

2.2 Equations of Motion

After the launch vehicle clears the dense atmosphere, the three-dimensional point-mass equations of motion in vacuum are:

$$\begin{aligned} \dot{\bar{r}} &= \bar{V} \\ \dot{\bar{V}} &= \bar{g} + \frac{T}{m}\hat{u}_T \\ \dot{m} &= -\frac{T}{g_0 I_{sp}} \end{aligned} \tag{2.1}$$

where $\bar{r}$ is the vehicle position in the inertial reference frame, $\bar{V}$ is the inertial velocity in the inertial reference frame, $\bar{g}$ is the gravitational acceleration, T is the engine thrust magnitude, and $\hat{u}_T$ is the unit vector which defines the direction of the thrust vector. The vehicle mass rate, $\dot{m}$, is a function of the engine thrust, the magnitude of the gravity vector, g_0, at some reference radius, R_0, and the specific impulse of the engine I_{sp}.

2.3 Aerodynamic Heating Rate Constraint

The simulation includes an evaluation of the free-molecular heat rate (FMHR) constraint at the time of payload fairing jettison:

$$FMHR = c\bar{q}V_{rel} \tag{2.2}$$

where c = 0.00128593 is an empirical constant. Dynamic pressure ($\bar{q}$) is dependent on current flight conditions and is calculated from atmospheric density (ρ) and relative velocity (V_{rel}):

$$\bar{q} = \frac{1}{2}\rho V_{rel}^2 \tag{2.3}$$

The relative velocity is calculated from the difference in the inertial velocity ($\bar{V}$) and the cross product between the rotation rate of the Earth ($\bar{\omega}_E$) and the inertial position ($\bar{r}$).

$$\bar{V}_{rel} = \bar{V} - \left(\bar{\omega}_E \times \bar{r}\right) \tag{2.4}$$

The rotation rate of the Earth is defined as $\bar{\omega}_E = \begin{bmatrix} 0 & 0 & \omega_{rate} \end{bmatrix}^T$ where the Earth rate (ω_{rate}) is 7.2921159(10^{-5}) rad/s. Then the magnitude of the relative velocity is:

$$V_{rel} = \left\| \bar{V}_{rel} \right\| \tag{2.5}$$

Note that atmospheric density is a function of altitude and is determined by the Earth Atmosphere Model, which is described in more detail in a later section.

2.4 Reference Coordinate Frames

There are a number of ways to define a coordinate frame, and those that pertain to this thesis are described below and illustrated in Figure 2.1. They are all right-handed, rectangular Cartesian axes.

Inertial Reference Frame ($\hat{i}_i, \hat{j}_i, \hat{k}_i$): a non-rotating, Earth-centered frame. The $\hat{k}_i$ axis points towards the North Pole. The $\hat{i}_i$ axis points towards the point on the Earth's surface with zero longitude at time $t = 0$ (time at start of ascent). The $\hat{j}_i$ axis completes the right-handed set.

Relative-Velocity Reference Frame ($\hat{i}_{rel}, \hat{j}_{rel}, \hat{k}_{rel}$): a frame centered at the vehicle's center of gravity (CG), which references the vehicle's motion to the motion of the surrounding air. The $\hat{i}_{rel}$ axis points along the wind-relative velocity vector, $\overline{V}_{rel}$. The $\hat{j}_{rel}$ axis is in the "local horizontal" plane (i.e. perpendicular to the inertial radius vector, $\overline{r}_i$). The $\hat{k}_{rel}$ axis completes the right-handed set such that it is pointing "upward" (i.e. away from the Earth.)

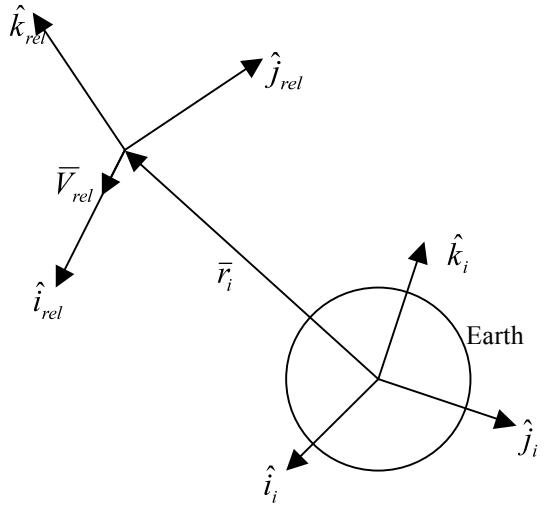

Figure 2.1: Coordinate Reference Frames

2.5 Coordinate Transformations

Converting a vector from one coordinate frame to another can be accomplished by some combination of rotation, translation, and scaling in order to match the orientation, origin of the new coordinate frame, and magnitude of the vector. Only rotational transformations must be considered here, for the following two reasons:

1. The non-inertial frames (which are accelerating with respect to the inertial frame) are centered at the vehicle's CG, which is where the accelerations are applied.
2. The only vectors for which transformations are made are acceleration vectors, which deal with changes in velocity rather than with velocities themselves.

A rotational transformation is accomplished by taking the matrix product of the original vector ($\bar{b}_1$) with the basis vectors for the old frame ($\hat{i}_1, \hat{j}_1, \hat{k}_1$) as expressed in the new frame. This yields the components for the new vector in the new frame ($\bar{b}_2$). Matrix notation is an effective representation, where the basis vectors for the new frame are combined into a transformation matrix ($T_{2\leftarrow 1}$).

$$\bar{b}_2 = \begin{bmatrix} \uparrow & \uparrow & \uparrow \\ (\hat{i}_1)_2 & (\hat{j}_1)_2 & (\hat{k}_1)_2 \\ \downarrow & \downarrow & \downarrow \end{bmatrix} \bar{b}_1 = T_{2\leftarrow 1}\bar{b}_1 \tag{2.6}$$

For this notation, vectors are considered column vectors unless otherwise stated. The reverse transformation ($\vec{b}_2$ to $\bar{b}_1$) can be calculated by using the inverse of the previously determined transformation matrix. Since the matrix is composed of mutually orthogonal unit vectors, the matrix is orthonormal, thus the inverse is equivalent to the matrix transpose:

$$\bar{b}_1 = T_{2\leftarrow 1}^{-1}\bar{b}_2 = T_{2\leftarrow 1}^{T}\bar{b}_2 \tag{2.7}$$

The transformation from relative velocity to the inertial frame is used to develop the equations of motion and heat rate constraint.

Relative-Velocity to Inertial Transformation: The vectors which form the transformation matrix are the basis vectors of the relative velocity frame, as expressed in the inertial frame.

$$T_{i\leftarrow rel} = \begin{bmatrix} \uparrow & \uparrow & \uparrow \\ \left(\hat{i}_{rel}\right)_i & \left(\hat{j}_{rel}\right)_i & \left(\hat{k}_{rel}\right)_i \\ \downarrow & \downarrow & \downarrow \end{bmatrix} \tag{2.8}$$

where

$$\left(\hat{i}_{rel}\right)_i = \frac{\left(\bar{V}_{rel}\right)_i}{V_{rel}} \tag{2.9}$$

$$\left(\hat{j}_{rel}\right)_i = \frac{\bar{r}_i \times \left(\bar{V}_{rel}\right)_i}{\left|\bar{r}_i \times \left(\bar{V}_{rel}\right)_i\right|} \tag{2.10}$$

$$\left(\hat{k}_{rel}\right)_i = \left(\hat{i}_{rel}\right)_i \times \left(\hat{j}_{rel}\right)_i \tag{2.11}$$

2.6 Environmental Models

The atmospheric model and gravity model defined in this section are empirical descriptions of the Earth environment, from which forces on the vehicle can be derived. This allows the simulation to yield results which accurately represent the real dynamics of the vehicle.

2.6.1 Earth Atmosphere Model

The atmospheric model used in the simulation environment is the Patrick 63 Atmosphere Model, which represents a simplified model of the mean atmosphere at Kennedy Space Center. The model, a function of geodetic altitude, evaluates density as a function of the input altitude, using a set of base densities and altitudes (ρ_{ref} and h_{ref}) and scale heights (h_{scale}).

$$\rho = \rho_{ref} \exp\left({h - h_{ref}} \Big/ {h_{scale}} \right) \tag{2.12}$$

For the purposes of this thesis, only the vacuum portion of ascent flight will be considered. Therefore, there are no aerodynamic forces and the density calculation is only used to evaluate the heat rate constraint at the jettison event.

2.6.2 Earth Gravity Model

The gravitational acceleration used in the simulation environment comes from a simple inverse-square relation, where gravity acts in the direction opposite the radius vector:

$$\bar{g}(r) = -\frac{\mu_E}{r^3}\bar{r} \tag{2.13}$$

where μ_E = 3.986 x 10^{14} m^3/s^2 is the gravitational parameter of the Earth and r is the magnitude of the position vector, $\bar{r}$. This gravitational acceleration formulation does not take into account the distortional effects due to a non-spherical Earth.

2.7 Simplified Vehicle Model

In order to simplify the vehicle description, the following assumptions are made in the development of the guidance algorithm:

1. The initial conditions $(\bar{r}_0, \bar{V}_0)$ are given.
2. Aerodynamic forces are neglected (i.e. vacuum flight).
3. The thrust magnitude (T), vehicle mass rate ($\dot{m}$), and exhaust velocity (V_{ex}) are piece-wise constant.
4. The gravitational acceleration vector varies as a linear function of the position vector.

Assumptions 2 and 3, along with linear steering, allows a closed-form solution for the thrust integral and requires no numerical integration or quadrature [16]. Another practical assumption is that the burn time for Stage 1, based on propellant loading and mass-flow rate, is fixed. The burn time for Stage 2, including the time at payload fairing jettison, is a parameter for optimization. Therefore, the final time for the complete trajectory (t_f) is free. Assumption 4 yields a closed-form solution of the costate equation and will be discussed in further detail in the next chapter.

2.8 Simulation Initialization

The trajectory generated by integrating the equations of motion depends on the vehicle's state at the start of simulation, which occurs after the initial separation of the solid rocket boosters. The vehicle state at simulation initialization will be specified by the vehicle characteristics and conditions taken from the OTIS design and mission profile for the Ares V CaLV.

2.8.1 Initial Position

By definition of the inertial reference frame (refer to Section 2.5), the initial position vector can be defined in terms of latitude (ϕ), longitude (δ).

$$\bar{r}(0) = \begin{bmatrix} \cos\delta\cos\phi \\ \sin\delta\cos\phi \\ \sin\phi \end{bmatrix} \tag{2.14}$$

Equation (2.14) determines the direction of the inertial position vector. Altitude (h) varies as a function of the position ($\bar{r}(0)$) and latitude (ϕ):

$$h = r_0 - (1-\varepsilon)\frac{r_E}{\sqrt{1+((1-\varepsilon)^2-1)}}(1-\sin\phi^2) \tag{2.15}$$

such that oblateness of the Earth is taken into account and the Earth flattening rate (ε) is determined by:

$$\varepsilon = \frac{r_{E,equatorial} - r_{E,polar}}{r_{E,equitorial}} \tag{2.16}$$

where $r_{E,equitorial}$ is 6,378,140 m and $r_{E,polar}$ is 6,356,750 m.

Then, in conjunction with the simulation initialization from the OTIS mission profile, the inertial position vector is:

$$\bar{r}(t_0) = \begin{bmatrix} -5{,}255{,}758 \\ -2{,}044{,}694 \\ 3{,}058{,}330 \end{bmatrix} \text{ m} \tag{2.17}$$

2.8.2 Initial Velocity

The direction of the velocity can be varied, and is described in terms of an azimuth (β) and flight-path angle (γ). Based on these parameters and the initial position, the direction of the velocity vector may be calculated by:

$$\bar{V} = \left(\bar{r} \times (\hat{k} \times \bar{r}) \cos\beta + (\hat{k} \times \bar{r}) \sin\beta\right) \cos\gamma + \bar{r} \sin\gamma \tag{2.18}$$

Applying the azimuth, flight path angle, and position, specified by the OTIS mission profile, Equation (2.18) yields the following initial velocity vector:

$$\bar{V}(t_0) = \begin{bmatrix} 413.927 \\ -1839.599 \\ 202.550 \end{bmatrix} \text{ m/s} \tag{2.19}$$

2.8.3 Target Location Specification

In order to evaluate guidance performance, it is necessary to specify a target location, which is referred to in this thesis as MECO. Guidance requires the target location in terms of the magnitude of the target's inertial position (r), velocity (V), flight path angle (γ), and inclination angle (i). Refer to Fig. 1.3, which depicts the major events from launch to MECO conditions. The simulation initialization parameters taken from the OTIS profile are summarized in Table 2.1.

Table 2.1: Summary of simulation initialization parameters

Parameter	Initial	Target
r	6,415,383 m	6,518,889 m
V	1896.441 m/s	7840.675 m/s
γ	10.6 deg	1.0064 deg
i	28.5 deg	28.5 deg

The magnitude of the initial inertial position and velocity (r and V) evolve from the vectors previously stated in Equations (2.17) and (2.19).

2.8.4 Vehicle Properties

The vehicle properties for the Ares V CaLV at each staging point are also denoted in Figure 1.3 and are summarized in Table 2.2.

Table 2.2: Summary of vehicle properties.

Event	Parameter	Value
Start of Simulation	mission elapsed time, t_0	155.9 s
Start of Simulation	vehicle mass, m_{01}	1,227,734 kg
Start of Simulation	vehicle thrust, T_1	17,437,041 N
Start of Simulation	engine specific impulse, Isp_1	414.7 s
Staging Point	mission elapsed time, t_{stage}	337.15 s
Staging Point	vehicle mass, m_{02}	307,837 kg
Staging Point	vehicle thrust, T_2	1,306,665 N
Staging Point	engine specific impulse, Isp_{12}	448 sec
PLF Jettison	mission elapsed time, t_{jett}	free
PLF Jettison	mass of PLF, m_{plf}	5,837 kg

The subscript 1 pertains to vehicle parameters for the RS-68 engine burn for stage 1, which has a fixed burn time. Similarly, the subscript 2 pertains to vehicle parameters during the J-2X burn for Stage 2, where the initialized mass for stage 2 (m_{02}) includes the RS-68 engine separation. The PLF jettison event also occurs during stage 2, where the time of jettison (t_{PLF}) is an optimization parameter and the burn time for stage 2 is free, thus the total flight time, t_f is free.

Chapter 3

Nominal Ascent Guidance Formulation

3.1 Overview

This chapter will present an off-line solution method, that is, a solution that is not in "real-time," for the optimal vacuum ascent problem. Based on optimal control theory, the costate solution can be expressed in closed-form and the state propagation can be expressed in an analytical solution derived from closed-form thrust integrals where the gravity integral is obtained by using a numerical predictor-corrector step. A simplification to the full costate applies direct parameter optimization through a gradient-based Matlab optimization toolbox to determine the optimal control during vacuum flight.

3.2 Optimal Control Theory: Problem Statement

As the traditional PEG and IGM guidance methods were developed from optimal control theory, it is necessary to define the two-point boundary-value problem for the rocket optimization problem. The equations of motion have been presented in Chapter 2 and can be recalled from Equation 2.1. At the time of main engine cutoff, t_f, k terminal state constraints are imposed:

$$\begin{aligned} &\Psi_i = \Psi_i(\bar{r}_D, \bar{V}_D) = 0 \\ &i = 1,...,k \qquad k \le 6 \end{aligned} \tag{3.1}$$

Examples of terminal constraints, which are nonlinear functions of the states, include final position magnitude (r), flight-path angle (γ), inclination (i), semi-major axis (a),

argument of perigee (ω), and longitude of ascending node (Ω). In addition to the terminal state constraints, the vehicle must also meet the interior state constraint:

$$N = N(\bar{r}_{PLF}, \bar{V}_{PLF}) = 1.135x10^3 \text{ J/ft}^2\text{/s} \tag{3.2}$$

defined by the *FMHR* constraint at the jettison event, evaluated with Eq. (2.2).

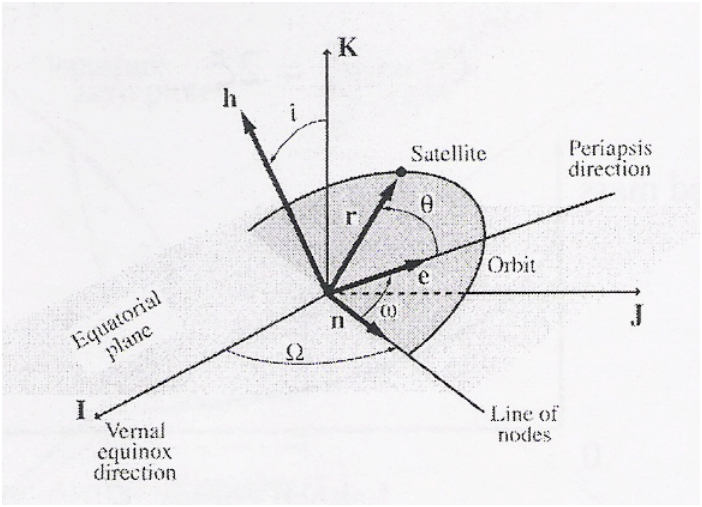

Figure 3.1: Classical orbital elements in the Earth-centered inertial (ECI) frame.

Figure 3.1 depicts the classical orbital elements, where the angular momentum ($\bar{h}$) is the cross product between the position and velocity vectors. The optimal thrust direction vector, $\hat{u}_T$, is determined by the solution of the optimal control problem that minimizes the performance index

$$J = -\int_{t_0}^{t_f} \dot{m}dt = \int_{t_0}^{t_f} \frac{T}{g_0 I_{sp}} dt \tag{3.3}$$

Recognizing that Eq. (3.3) integrates a set of constants, the optimal control attempts to minimize the final time, $J = t_f$. In addition to the terminal state constraints, the vehicle must also meet the free molecular heat-rate constraint at the PLF jettison event, previously defined in Chapter 2. Thus, the optimization problem can be stated as

follows: Determine the optimal control (thrust direction) that minimizes the flight time (equivalent to maximizing the final vehicle mass) subject to the equations of motion [Eq. (2.1)], terminal constraints [Eq. (3.1)], and interior state constraint [Eq. (3.2)].

3.3 Vacuum Guidance Formulation

The analytical vacuum optimal ascent guidance solution combines results from several vacuum trajectory studies performed over the past three decades (summarized in Refs. 10 and 12) and is shown here for completeness. A key factor in developing the analytic vacuum solution is the linear gravity approximation, which enables a closed-form solution to the costate equation. The gravitational acceleration can be approximated by the so-called linear central gravity field:

$$\bar{g}(\bar{r}) \cong -\frac{\mu_E}{r_0^3}\bar{r} \equiv -\omega_0^2\bar{r} \tag{3.4}$$

where $\omega_0 = \mu_E / r_0^3$ is the Schuler frequency. This approximation allows for the preservation of the direction of gravity, which for ascent flight, is more important than the accuracy of its magnitude.

Table 3.1: Numerical comparison of gravity calculation

	Inverse-Square μ_E/r^2	Linear $\omega_0^2 r$
$t = t_0$	9.685 m/s^2	1.46E-08 m/s^2
$t = t_{stage}$	9.418 m/s^2	1.36E-08 m/s^2
$t = t_f$	9.380 m/s^2	1.35E-08 m/s^2

Table 3.1 compares the numerical values of gravity by evaluating the term with both the inverse-square model and linear model. The linear approximation causes a difference in

the magnitude of $\bar{g}$, but as r_0 is continuously updated by the radius at the beginning of each guidance cycle, the effect of the difference carries little influence on the validity of the solution.

3.3.1 Optimality Condition

Following standard optimal control theory [17], the Hamiltonian is defined as:

$$H = L + \bar{\lambda}^T \bar{f} \tag{3.5}$$

Since $L = 0$, Eq. (3.5) simplifies to:

$$H = \bar{\lambda}^T \bar{f} \tag{3.6}$$

for the rocket optimization problem, where vector $\bar{f}$ represents the equations of motion. The Hamiltonian expansion yields:

$$H = \bar{\lambda}_r^T \bar{V} + \bar{\lambda}_V^T \left[-\bar{g} + \frac{T}{m} \hat{u}_T \right] + \eta \left(\hat{u}_T^T \hat{u}_T - 1 \right) \tag{3.7}$$

where η is a scalar multiplier and $\bar{\lambda}_r$ and $\bar{\lambda}_V$ are the costate vectors. The first two terms correspond to the right-hand side of the $\dot{\bar{r}}$ and $\dot{\bar{V}}$ equations of motion, while the third term is included to constrain the control such that it is in fact a unit vector. The optimality condition is derived by applying the maximum principle to the Hamiltonian, which results in the optimization sub-problem:

$$H\left(\bar{\lambda}_r, \bar{\lambda}_V, \bar{r}^*, \bar{V}^*, \hat{u}_T^*, t\right) = \max_{\hat{u}_T} H\left(\bar{\lambda}_r, \bar{\lambda}_V, \bar{r}^*, \bar{V}^*, \hat{u}_T, t\right) \tag{3.8}$$

where the asterisks denote the optimal values for the associated variables. Applying the optimality condition:

$$\frac{\partial H}{\partial \hat{u}_T} = 0 \tag{3.9}$$

the optimal control becomes

$$\hat{u}_T^* = -\frac{T}{2\eta m}\bar{\lambda}_V \tag{3.10}$$

Expanding Eq. (3.13),

$$\hat{u}_T^T \hat{u}_T = \frac{T^2}{4\eta^2 m^2}\bar{\lambda}_V^T \bar{\lambda}_V = 1 \tag{3.11}$$

$$\therefore \left(\frac{T}{2\eta m}\right)^{-1} = \left\|\bar{\lambda}_V\right\| = \frac{2\eta m}{T} \tag{3.12}$$

and the scalar multiplier is:

$$\eta = \frac{-T}{2m}\left\|\bar{\lambda}_V\right\| \tag{3.13}$$

Thus, $\eta < 0$, and substituting Eq. (3.13) into Eq. (3.10)

$$\hat{u}_T^* = +\frac{\bar{\lambda}_V}{\left\|\bar{\lambda}_V\right\|} \tag{3.14}$$

results in the well known result that the optimal thrust direction unit vector must be aligned with the fuel-optimum vector ($\bar{\lambda}_V$), also known as the primer vector [18].

3.3.2 Costate Differential Equations

Based on the Hamiltonian in Eq. (3.7), the costate equations are defined as:

$$\dot{\bar{\lambda}} = -\frac{\partial H}{\partial \bar{x}} \tag{3.15}$$

Substituting the linear central gravity field assumption, Eq. (3.4), the costate differential equations can be written as:

$$\dot{\bar{\lambda}}_r = -\frac{\partial H}{\partial \bar{r}} = \omega_0^2 \bar{\lambda}_V \tag{3.16}$$

$$\dot{\bar{\lambda}}_V = -\frac{\partial H}{\partial \bar{V}} = -\bar{\lambda}_r \tag{3.17}$$

where Eq. (3.17) indicates that the control rate is negative. To obtain the closed-form solution to the position costate equation,

$$\ddot{\bar{\lambda}}_r = \omega_0^2 \dot{\bar{\lambda}}_V = -\omega_0^2 \bar{\lambda}_r \tag{3.18}$$

Rearranging Eq. (3.18) produces the form of an undamped harmonic oscillator,

$$\ddot{\bar{\lambda}}_r + \omega_0^2 \bar{\lambda}_r = 0 \tag{3.19}$$

whose solution is:

$$\bar{\lambda}_r(t) = \bar{\lambda}_r(t_0)\cos\omega_0 t + \bar{\lambda}_V(t_0)\omega_0 \sin\omega_0 t \tag{3.20}$$

The velocity costate is:

$$\bar{\lambda}_V(t) = -\int_0^t \bar{\lambda}_r dt = -\frac{\bar{\lambda}_{r0}}{\omega_0}\sin\omega_0 t + \bar{\lambda}_{V0}\cos\omega_0 t \tag{3.21}$$

where $\bar{\lambda}_{r0}$ and $\bar{\lambda}_{V0}$ are the unknown initial conditions for the costate.

Analytical solutions to the state equations also exist and utilize the closed-form thrust integrals, I_c and I_s, which assume constant thrust magnitude and linear steering, and have the form:

$$I_c(t) = \int_0^t \hat{u}_{\lambda_V}(t) a_T(t)\cos\omega_0 t dt \overset{\Delta}{=} \int_{t_0}^t \dot{I}_c(t) dt \tag{3.22}$$

$$I_S(t) = \int_0^t \hat{u}_{\lambda_V}(t) a_T(t) \sin \omega_0 t dt \overset{\Delta}{=} \int_{t_0}^t \dot{I}_S(t) dt \tag{3.23}$$

where $\hat{u}_{\lambda_V} = \bar{\lambda}_V / \left\| \bar{\lambda}_V \right\|$. Note, the thrust acceleration $a_T(t)$ is time-varying due to the changing mass.

$$a_T(t) = \frac{T}{m_0 - \dot{m}t} \tag{3.24}$$

Calise et al. use Simpson's rule to develop the thrust integral solutions [12], while Lu et al. use Milne's rule, which offers a significantly higher precision [10]. In general, the thrust integrals first compute the new velocity based on the thrust force and constant gravity. Then the gravity term, following the inverse-square relation, is added to propagate the predicted position and velocity. The gravity is then calculated at the new predicted position. An average gravity vector is formed over the entire burn and is used to update the propagated position and velocity vectors.

The state equations:

$$\bar{r}(t) = \int_{t_0}^t \bar{V} dt \tag{3.25}$$

$$\bar{V}(t) = \int_{t_0}^t \left(\bar{g}(t) + a_T \hat{u}_T \right) dt \tag{3.26}$$

can be shown to have the solution [19]:

$$\begin{bmatrix} \bar{r} \\ \bar{V} \end{bmatrix} = \Omega \begin{bmatrix} \bar{r}_0 \\ \bar{V}_0 \end{bmatrix} + \Gamma \begin{bmatrix} I_c \\ I_s \end{bmatrix} \tag{3.27}$$

where Ω is a 2 x 2 matrix consisting of the costate solution coefficients:

$$\Omega = \begin{bmatrix} \cos \omega_0 t & \sin \omega_0 t \\ -\sin \omega_0 t & \cos \omega_0 t \end{bmatrix} \tag{3.28}$$

and

$$\Gamma = \frac{1}{\omega_0}\begin{bmatrix} \sin\omega_0 t & -\cos\omega_0 t \\ \cos\omega_0 t & \sin\omega_0 t \end{bmatrix} \tag{3.29}$$

From the costate solutions and thrust integrals in Equations (3.20)-(3.23) and the state equation in Equation (3.27), it is determined that the final states and costates are explicit functions of the initial costates, $\bar{\lambda}_{r0}$ and $\bar{\lambda}_{V0}$.

3.3.3 Transversality Conditions

The transversality conditions are conditions on the final costate and final Hamiltonian:

$$\begin{aligned} \bar{\lambda}_f &= \bar{\lambda}(t_f) = \bar{v}^T \bar{\Psi} \\ H_f &= H(t_f) = 1 \end{aligned} \tag{3.30}$$

where $\bar{v}$ is a column-vector of constant Lagrange multipliers. The second condition is relevant for cases in which the final time (t_f) is not specified. A detailed discussion of the transversality conditions is given in Ref. 9, in which the satisfaction of the transversality conditions imply that the Keplerian part of the final Hamiltonian is zero.

For the minimum-time problem, the initial costates are not completely independent, as they can be arbitrarily scaled by a positive constant without changing the necessary conditions for the optimal control problem. For example, the costates may be scaled such that

$$\left\| \bar{\lambda}_0^T \right\| = \left\| \begin{matrix} \bar{\lambda}_{V0}^T \\ \bar{\lambda}_{r0}^T \end{matrix} \right\| = 1 \tag{3.31}$$

where just one of the 6 components of $\bar{\lambda}_0$ can be determined by the rest. To avoid the issue of determining the sign of $\bar{\lambda}_0$, the problem may be treated as a problem with seven-unknowns, where the seventh unknown is the free final time, t_f. Then the condition on the final costates,

$$\left\|\bar{\lambda}_f\right\| = 1 \tag{3.32}$$

becomes the seventh terminal condition, a simple, non-constraining condition.

To summarize, the minimum-time, vacuum ascent guidance problem is formulated as a root-finding problem:

$$\begin{aligned} &\min_{\hat{u}_T} t_f \\ \text{s.t.} \quad &\Psi_i = \Psi_i(\bar{r}_D, \bar{V}_D) = 0 \\ &i = 1,\ldots,k \qquad k \le 6 \\ &N = N(\bar{r}_{PLF}, \bar{V}_{PLF}) = FMHR \end{aligned} \tag{3.33}$$

with seven unknowns made up of the initial costate ($\bar{\lambda}_0$) and the final time (t_f). As previously shown, the final states ($\bar{x}_f$) and costates ($\bar{\lambda}_f$) are explicit function of the seven unknowns and the optimal control unit vector ($\hat{u}_T^*$) is in the direction of $\bar{\lambda}_{V0}$.

3.4 Numerical Solution Method

A typical solution approach to the two-point boundary-value problem is the shooting method outlined by Bryson and Ho [17]. The unknown costates and final flight time are the free variables that must be updated through iteration to meet the *k* terminal state constraints, optimality, and transversality conditions. The shooting method updates

the estimates of the unknown conditions by computing the Jacobian, a matrix of first-order partial derivatives, and the errors in the boundary conditions which result from that initial estimate.

3.4.1 Direct Parameter Optimization

The optimization problem can be greatly simplified by applying a direct parameter optimization method, which simplifies the full costate with the assumption of linear steering. Recall from the previous section that $\hat{u}_T^* = unit\left(\bar{\lambda}_V\right)$ and the solution to $\bar{\lambda}_V$ is a harmonic function. Also recall $\dot{\bar{\lambda}}_V = -\bar{\lambda}_r$ so that Eq. (3.21) may be rewritten as:

$$\bar{\lambda}_V(t) = \bar{\lambda}_{V0}\cos\omega_0 t + \frac{\dot{\bar{\lambda}}_{V0}}{\omega_0}\sin\omega_0 t \tag{3.34}$$

Recognizing that the orbital rate is very small, apply small angle assumptions, $\omega_0 t \to 0$, such that $\cos\omega_0 t \cong 1$ and $\sin\omega_0 t \cong \omega_0 t$, Eq. (3.34) may be simplified to the form:

$$\bar{\lambda}_V(t) = \bar{\lambda}_{V0} + \dot{\bar{\lambda}}_{V0} t \tag{3.35}$$

Then for a direct parameter optimization approach, the control unit vector assumes the form:

$$\hat{u}_T = \frac{\bar{A}t + \bar{B}}{\left\|\bar{A}t + \bar{B}\right\|} \tag{3.36}$$

where the steering parameters, $\bar{A}$ and $\bar{B}$, are related to the costates by:

$$\bar{A} \cong \dot{\bar{\lambda}}_{V0} = -\bar{\lambda}_{r0} \tag{3.37}$$

$$\bar{B} \cong \bar{\lambda}_{V0} \tag{3.38}$$

Recall from Chapter 2, the solution will consist of two burn stages: 1) a fixed-burn for stage 1, and 2) a free burn time for stage 2, where a heat-rate constraint must be met at the optimal payload fairing jettison time (t_{PLF}). Under the assumption of linear steering, and using the direct method, the optimization problem becomes:

$$\min_{\bar{A},\bar{B}} t_f$$

$$\begin{aligned} \text{s.t.} \quad & \Psi_i = \Psi_i(\bar{r}_D, \bar{V}_D) = 0 \\ & i = 1,\ldots,k \qquad k \le 6 \\ & N = N(\bar{r}_{PLF}, \bar{V}_{PLF}) = FMHR \end{aligned} \tag{3.39}$$

The optimal control desired for the entire ascent trajectory must maintain thrust-direction attitude continuity over the jettison event while also meeting the heat-rate constraint from Eq. (2.2) at the jettison time.

$$\hat{u}_T\left(t_{PLF}^-\right) = \hat{u}_T\left(t_{PLF}^+\right) \tag{3.40}$$

The continuity condition in Eq. (3.32) determines the thrust-direction parameters at PLF jettison, $\bar{B}_{PLF}$. Such a trajectory yields a total of 11 optimization parameters: 6 initial steering parameters, $\bar{A}_1 \in R^3$ and $\bar{B}_1 \in R^3$, three additional steering rates after jettison, $\bar{A}_{PLF} \in R^3$, jettison time, t_{PLF}, and the burn time from the jettison point to the MECO conditions, t_{burn}.

3.4.2 Choosing the Initial Control Parameters

An important consideration for optimization problems is choosing the initial control vector. For the indirect method that uses the full costate, the optimal impulsive solutions are a possibility and Kern [20] uses an optimal two-impulse solution to obtain

starting iterations for the control vector. Robbins [21] describes a technique to convert the impulses to finite burn arcs and Tarbet [22] uses a conjugate gradient algorithm instead of a weighted Newton-Raphson technique to obtain converged solutions.

This thesis provides an approach using a direct optimization method. In either case, the goal is to determine the vectors ($\overline{A}$ and $\overline{B}$) that define the thrust direction ($\hat{u}_T$). A reasonable guess for the initial steering direction:

$$\overline{B}_1 = \frac{\overline{V}(t_0)}{\left\|\overline{V}(t_0)\right\|} \tag{3.41}$$

such that the initial thrusting direction is approximately along the initial velocity vector. A reasonable guess for $\overline{A}$ is $\overline{A} = \begin{bmatrix} 10^{-4} & 10^{-4} & 10^{-4} \end{bmatrix}^T s^{-1}$, which are typically small values relative to $\overline{B}$. Recall from section 3.3.3, one component of $\overline{A}$ and $\overline{B}$ is arbitrary and $\overline{A}$ and $\overline{B}$ may be scaled by any positive factor without changing the solution. To aid in the guesswork for the steering parameters, a "non-constraining" constraint:

$$\left\|\overline{B}\right\| = 1 \tag{3.42}$$

ensures that the components will all be less than unity and allows for upper and lower bounds to be placed on the parameters during the optimization routine.

3.5 Analytical Costate Jump Condition

Another simplification to the optimization problem can be made by developing the analytical solution to the position costate jump condition at payload fairing jettison. Given an interior-point state constraint of the form:

$$N\left[\bar{x}(t),t\right]-N_{\lim}=0 \tag{3.43}$$

where N could be the FMHR constraint in Eq. (2.2), the necessary conditions are [17]:

$$\bar{\lambda}^{T}\left(t^{-}\right)=\bar{\lambda}_{T}\left(t^{+}\right)+\pi\frac{\partial N}{\partial\bar{x}} \tag{3.44}$$

$$H\left(t^{-}\right)=H\left(t^{+}\right)-\pi\frac{\partial N}{\partial t} \tag{3.45}$$

where (t^{-}) represents the time before the jettison event, and (t^{+}) represents the time immediately after the jettison event, and π is the jump condition. For the rocket optimization problem, continuous thrust-steering directions are desired, and the constraint is not an explicit function of time, so Eqs. (3.44) and (3.45) specialize to:

$$\bar{\lambda}_{r}^{T}\left(t^{-}\right)=\bar{\lambda}_{r}^{T}\left(t^{+}\right)+\pi\frac{\partial N}{\partial\bar{r}} \tag{3.46}$$

$$\bar{\lambda}_{V}^{T}\left(t^{-}\right)=\bar{\lambda}_{V}^{T}\left(t^{+}\right) \tag{3.47}$$

$$H\left(t^{-}\right)=H\left(t^{+}\right) \tag{3.48}$$

Expanding out the "continuity of Hamiltonian" condition:

$$\begin{aligned}&\left(\bar{\lambda}_{r}^{T}\bar{V}\right)^{-}+\lambda_{V}^{T}\left(\frac{T}{m}\hat{u}_{T}+\bar{g}\right)^{-}=\left(\bar{\lambda}_{r}^{T}\bar{V}\right)^{+}-\pi\bar{N}_{r}\bar{V}+\lambda_{V}^{T}\left(\frac{T}{m}\hat{u}_{T}+\bar{g}\right)^{+}\\&\Leftrightarrow\lambda_{V}^{T}\left(\frac{T}{m^{-}}\hat{u}_{T}\right)=-\pi\bar{N}_{r}\bar{V}+\lambda_{V}^{T}\left(\frac{T}{m^{+}}\hat{u}_{T}\right)\end{aligned} \tag{3.49}$$

The π parameter appears linearly in Eq. (3.49), and recognizing that the primer vector ($\bar{\lambda}_{V}$) is in the same direction as the control ($\hat{u}_{T}$), allows a solution in closed-form:

$$\pi=\frac{m_{PLF}\left\|\bar{\lambda}_{V}\right\|T}{m^{-}\left(m^{-}-m_{PLF}\right)\bar{N}_{r}^{T}\bar{V}} \tag{3.50}$$

Substituting this expression back into Eq. (3.46) gives a closed-form expression for the position costate at the time of payload fairing jettison:

$$\bar{\lambda}_r^T\left(t^+\right) = \bar{\lambda}_r^T\left(t^-\right) - \frac{m_{PLF}\left\|\bar{\lambda}_V\right\| T\bar{N}_r}{m^-\left(m^- - m_{PLF}\right)\bar{N}_r^T\bar{V}} \tag{3.51}$$

Recall that $\bar{\lambda}_r$ is really the rate of the primer vector, $\bar{\lambda}_r = -\dot{\bar{\lambda}}_V$, or equivalently, $\bar{\lambda}_r \cong \bar{A}$, so the position costate ($\bar{\lambda}_r$) should be discontinuous at the interior-point constraint (*N*). Therefore, there should be a change in the slope of the thrust-steering at the PLF jettison event seen in its time history. This expression makes intuitive sense. The lighter the payload fairing becomes, the less the change in $\bar{A}$ or $\bar{\lambda}_r$, which means that the presence of the constraint does not change the optimized trajectory from the unconstrained optimized trajectory. In other words, as the fairing becomes lighter and lighter, the optimal trajectory states will look more and more as if there were no constraint at all.

Note that the *N* here could represent a dynamic pressure constraint or as in this case, the heat-rate constraint. In either case, the same general form of the necessary condition applies and the new position costate is obtained in closed-form. This represents a direct advantage over the direct optimization method discussed in the previous section where the new position costate represents three additional parameters that must be optimized. The price paid for this benefit is the upfront analytical work and slightly more complicated coding. This includes determining the expression for the partial derivative of the constraint with respect to position ($\bar{N}_r$) and then writing the code to evaluate the derivative expression and the resulting jump in the costate at the jettison event.

Chapter 4

Results of the Off-line Optimization

4.1 Overview

Trajectory optimization routines have been developed that can easily test different guidance schemes. In particular, the routine can optimize a heat-rate constrained ascent trajectory in vacuum flight. This chapter investigates how the optimal control (thrust direction) may be found through a direct parameter optimization method, comparing the optimal trajectory solutions to the Ares V baseline guidance solutions demonstrated through OTIS.

4.2 Off-Line Trajectory Optimization

The direct parameter optimization method for the optimal control, discussed in Chapter 3, has been applied to three cases:

1. Nominal Optimal Trajectory: The nominal trajectory with 11 optimization parameters.
2. Test Case 1: The 14 parameter trajectory, where the additional 3 optimization parameters are the steering rates ($\overline{A}_{stage1}$) at the staging point.
3. Test Case 2: The 20 parameter trajectory, where the additional 9 optimization parameters are the steering rates and directions at the staging point and jettison point ($\overline{A}_{stage1}, \overline{B}_{stage1}, \overline{B}_{PLF}$).

Trajectory optimization routines were developed by creating Matlab functions (mfiles). The optimization routine utilizes Matlab's built-in function FMINCON.m, a gradient-

based function that performs constrained non-linear optimization. FMINCON.m attempts to find the constrained minimum of a scalar function of several variables starting at an initial estimate. The main advantage of the direct parameter optimization approach is that the math and coding is much simpler than the indirect approach.

4.2.1 Nominal Optimal Trajectory

The nominal optimal trajectory case includes 11 parameters for optimization: $\overline{A}_1$, $\overline{B}_1$, $\overline{A}_{PLF}$, t_{PLF}, and t_{burn}, where t_{burn} is the burn time from PLF jettison to the target conditions. The trajectory disregards any atmospheric flight portions of ascent, and is initialized during vacuum conditions. The reference trajectories (from OTIS) are available and comparison plots were made to verify acceptable performance of the optimization routine. A summary of the optimization results, as well as the corresponding results from OTIS are listed in Table 4.1.

Table 4.1: Summary of optimization results.

Parameter	OTIS	Optimization
t_{PLF} (s)	422.20	441.02
t_{burn} (s)	361.80	328.43
t_f (s)	784.00	769.45
m_f (kg)	166,630	173,430

The optimization results display better performance over OTIS, but do not model the RS-68 thrust tail-off or the J-2X start up transients, and assumes that the RS-68 burn has full thrust until J-2X start up. These thrust transients, however, may easily be modeled by evaluating the integral of the thrust-time curve where it is more important to match the area under the curve than to model the exact shape of the thrust-time curve. Figures 4.1

thru 4.6 show the important plots of the important trajectory parameters from the optimized results.

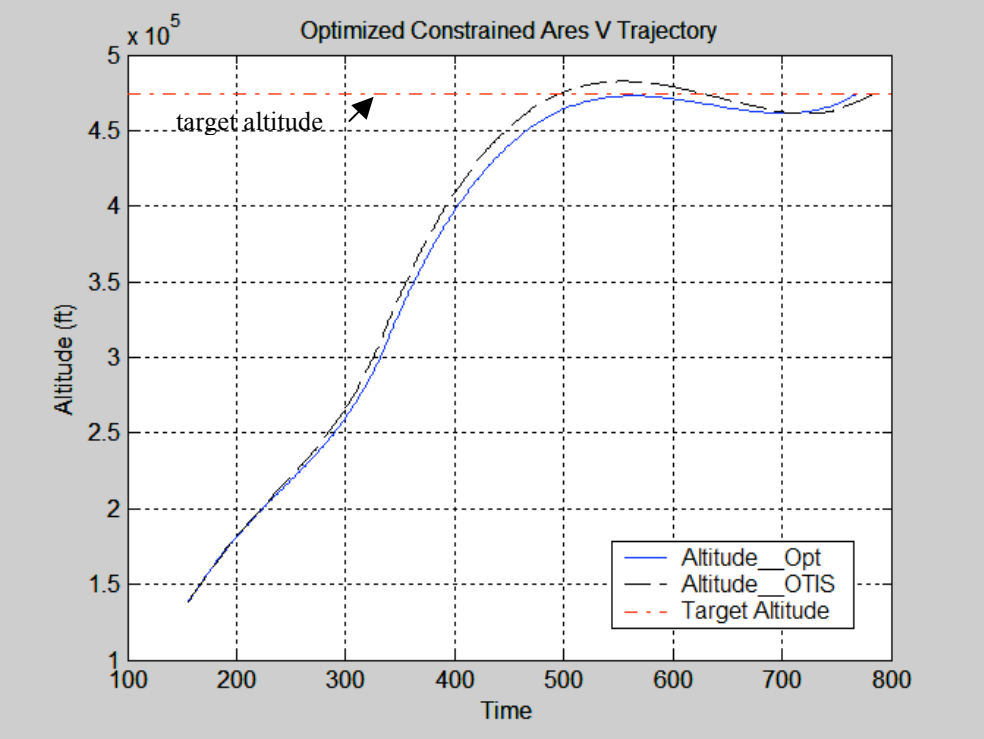

Figure 4.1: Plot of optimal altitude with OTIS comparison.

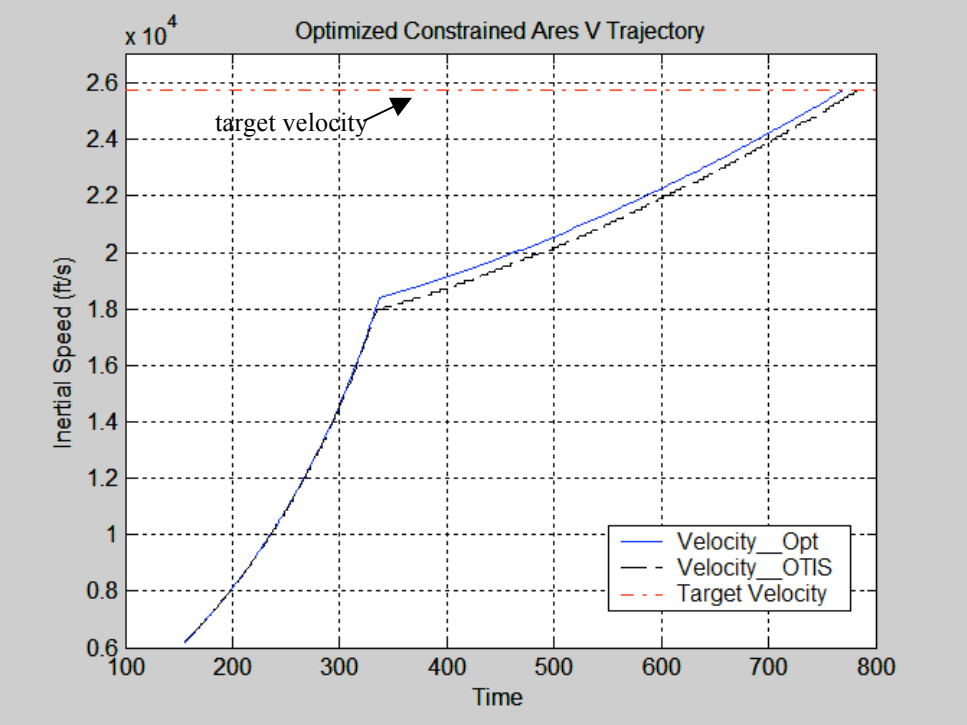

Figure 4.2: Plot of optimal inertial velocity with OTIS comparison.

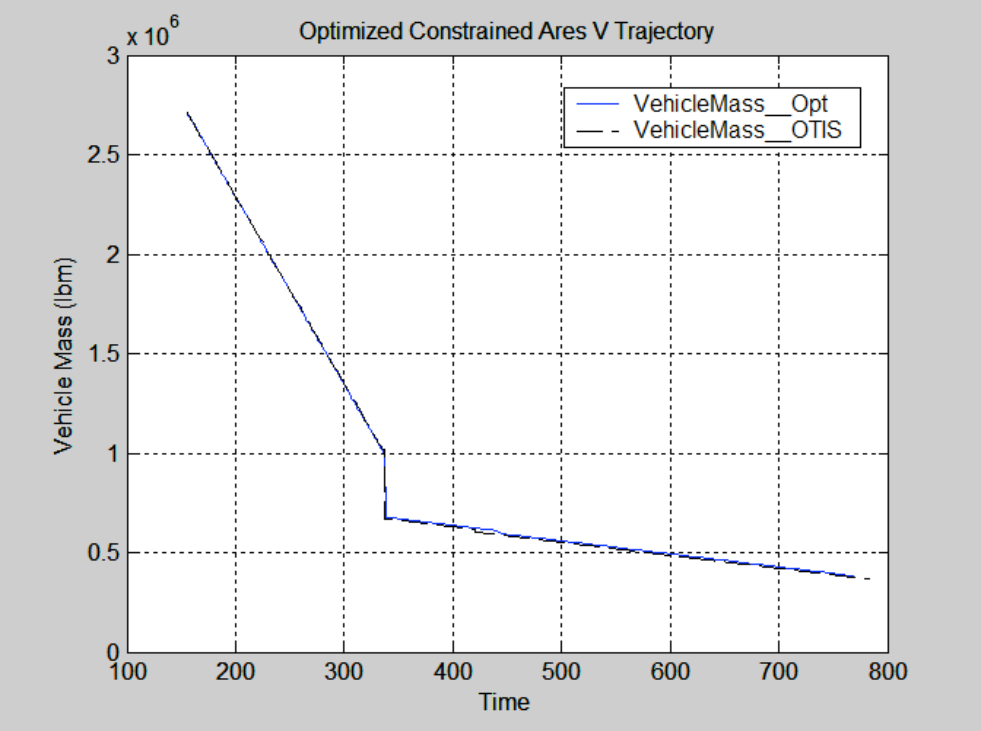

Figure 4.3: Plot of vehicle mass with OTIS comparison.

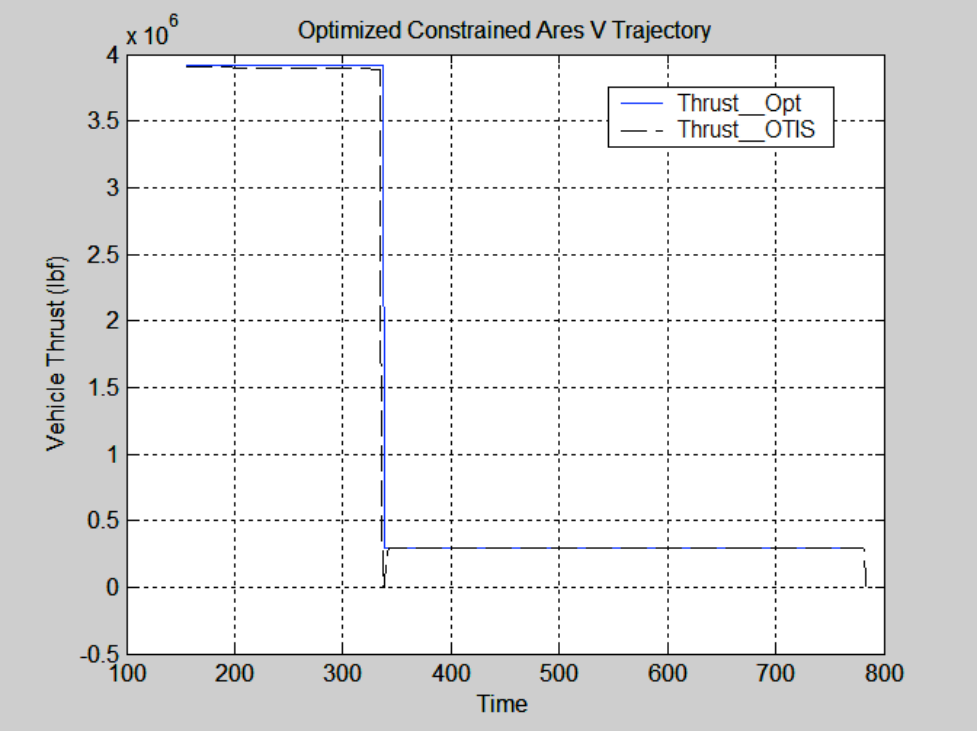

Figure 4.4: Plot of vehicle thrust with OTIS comparison.

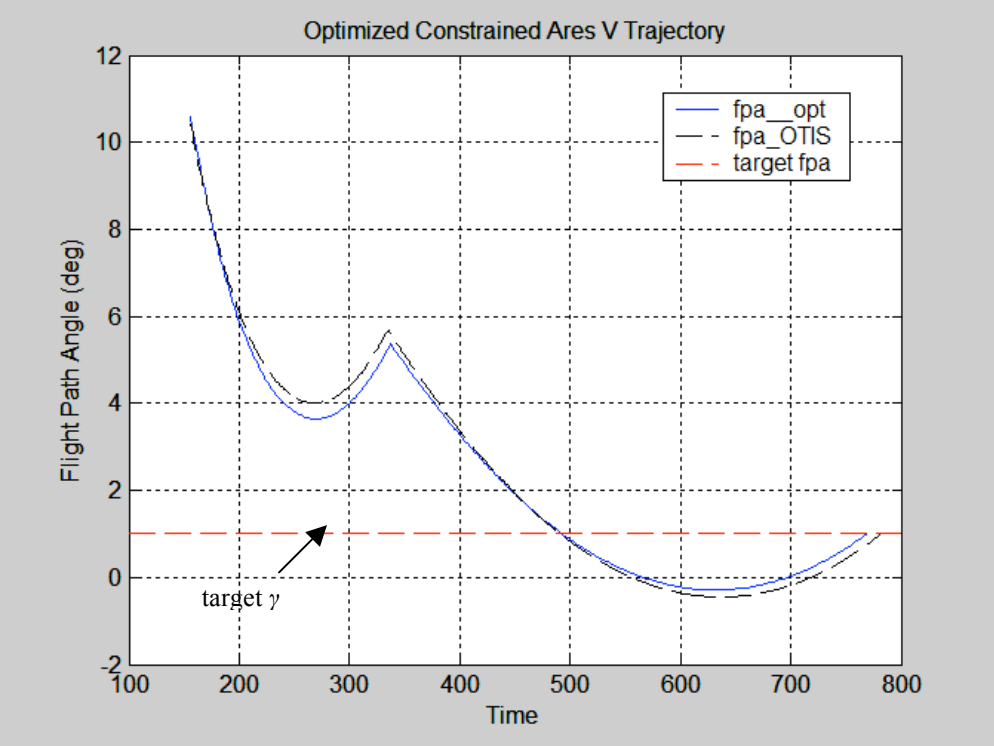

Figure 4.5: Plot of optimal flight path angle with OTIS comparison.

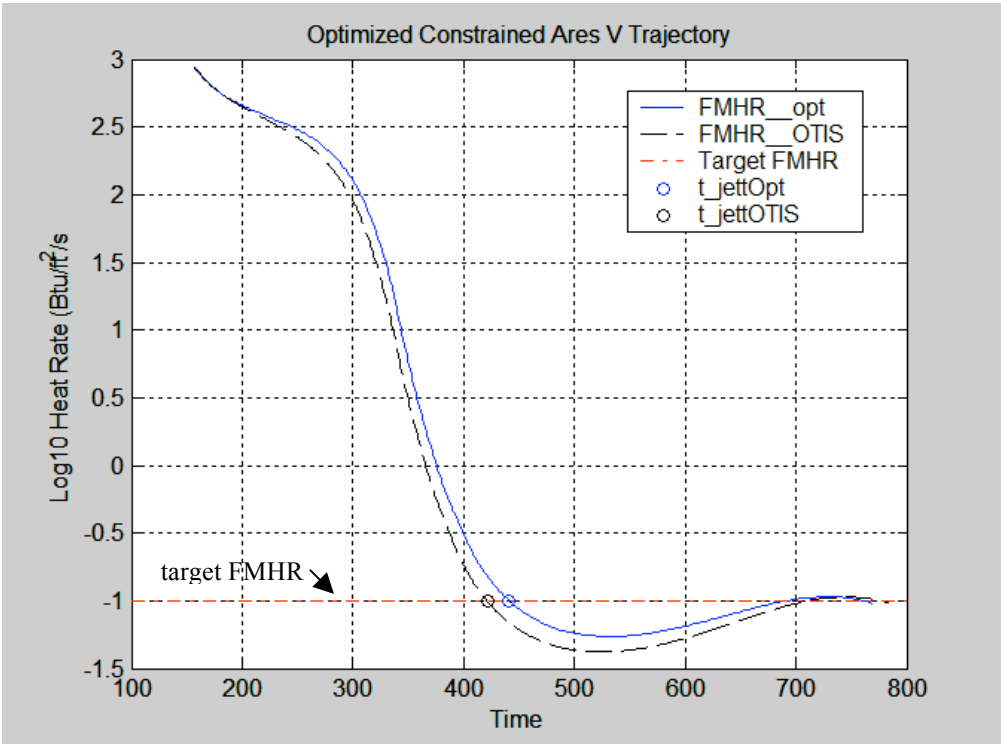

Figure 4.6: Plot of Free Molecular Heat Rate (FMHR) with OTIS comparison and jettison times denoted.

Figures 4.1 and 4.2 compare the ascent altitude and inertial velocity for the optimized trajectory and the reference OTIS trajectory. Notice that in Figs. 4.1, the OTIS simulation shows the lofting effect, which has been known to improve fuel performance. Although the histories in Figs. 4.1 and 4.2 are noticeably different in the middle of the trajectory, the final states from the optimization still converge to the desired target altitude and velocity. Figure 4.3 shows the vehicle mass histories and Figure 4.4 shows the vehicle thrust histories, where the modeling discrepancies and thrust transients which were disregarded in the optimization routine, are apparent. Figure 4.5 shows the optimal flight-path angle history for the trajectory. Figure 4.6 pertains to the heat-rate associated with ascent, and the heat-rates at jettison times for both the optimized results and OTIS results have been denoted. The second peak, which occurs after the heat-rate constraint has been met, is unavoidable. A solution to keep that peak below the heat-rate constraint, however, would be to raise the target conditions at MECO by a few thousand meters. In general, the trends displayed by the optimization routine are consistent with the reference OTIS trajectory, indicating that the results are sufficiently accurate and optimal.

4.2.2 Additional Degrees of Freedom

Although the optimal control for the rocket optimization problem is desired at the initial point of trajectory and across the jettison event, it is advantageous to impose additional degrees of freedom to the optimization problem. Allowing the optimizer to choose the additional steering parameters at the staging point and jettison point is a way to test and validate the assumption of linear steering.

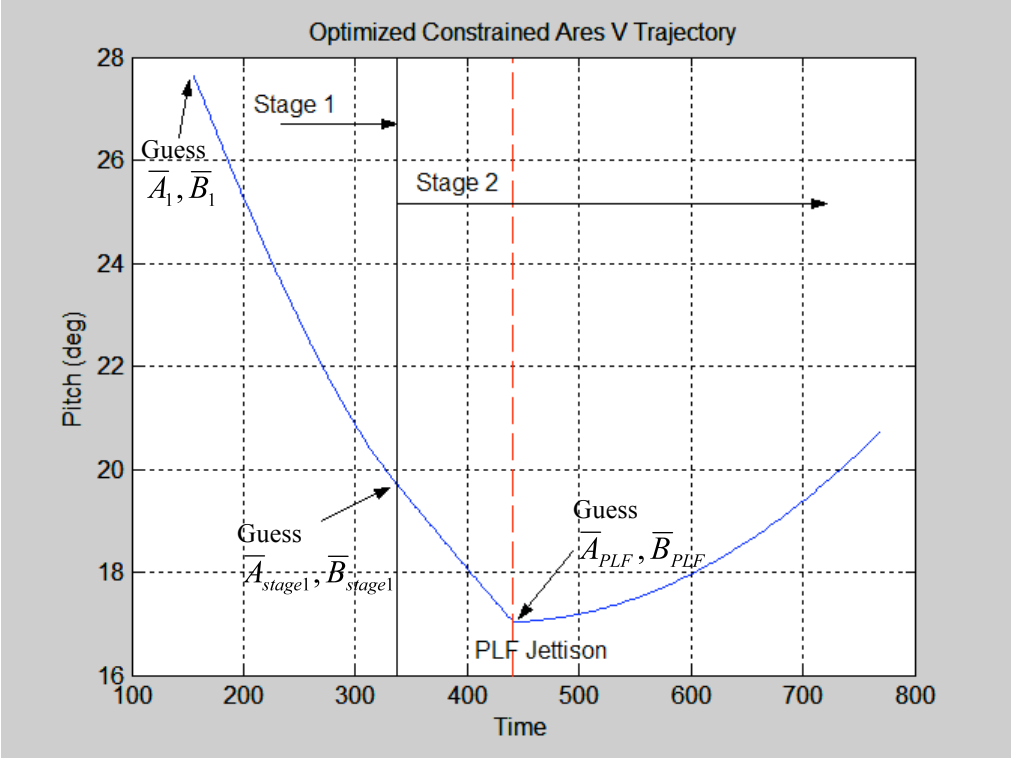

Figure 4.7: Pitch steering profile for nominal case with 11, 14, or 20 free parameters indicated.

Figure 4.7 is a plot of the pitch steering profile from the nominal optimized case and depicts the additional optimization parameters at the time of staging and time of payload fairing jettison. Pitch (θ) is measured positive from the horizon to the thrust vector and projected into the vertical plane.

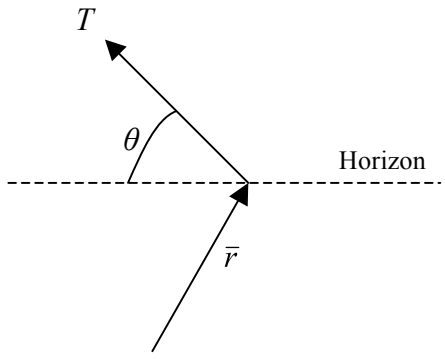

Figure 4.8: Depiction of pitch angle.

Note that the pitch profile does in fact display the anticipated discontinuous thrust-steering at the interior-point constraint (the PLF jettison) and Fig. 4.7 illustrates the

corresponding change in slope, previously discussed in chapter 3. The ascent trajectory was re-optimized, allowing the optimizer to choose 1) 3 additional steering rate parameters at the staging point, $\overline{A}_{stage1}$, for a total of 14 optimization parameters, and 2) 9 additional parameters for the steering rates and directions at the staging point and the jettison point, $\overline{A}_{stage1}$, $\overline{B}_{stage2}$, $\overline{B}_{PLF}$, for a total of 20 optimization parameters. Although test case 2 allows the optimizer to choose the thrust directions, $\overline{B}_{stage1}$ and $\overline{B}_{PLF}$, it is expected that these directions remain continuous across staging and jettison events, as defined by the continuity condition from Eq. (3.40).

Figures 4.9-4.14 illustrate the important trajectory parameters for the nominal case and the two test cases, and are again plotted along with the reference OTIS trajectory.

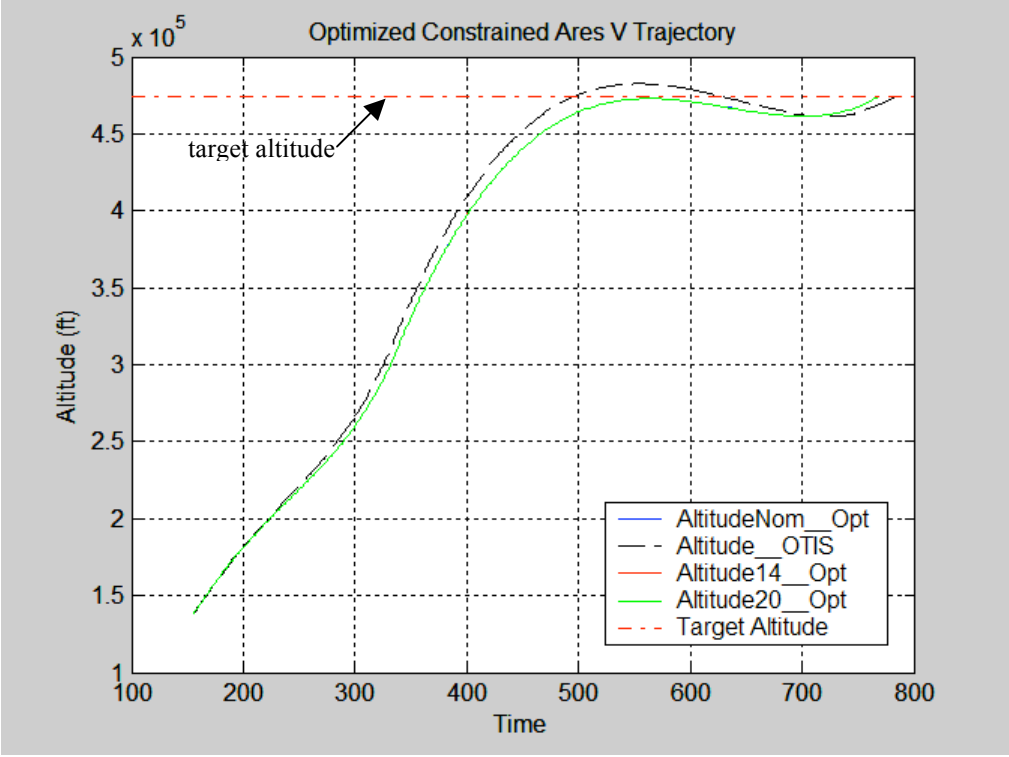

Figure 4.9: Plot of optimal altitudes for all test cases with OTIS comparison.

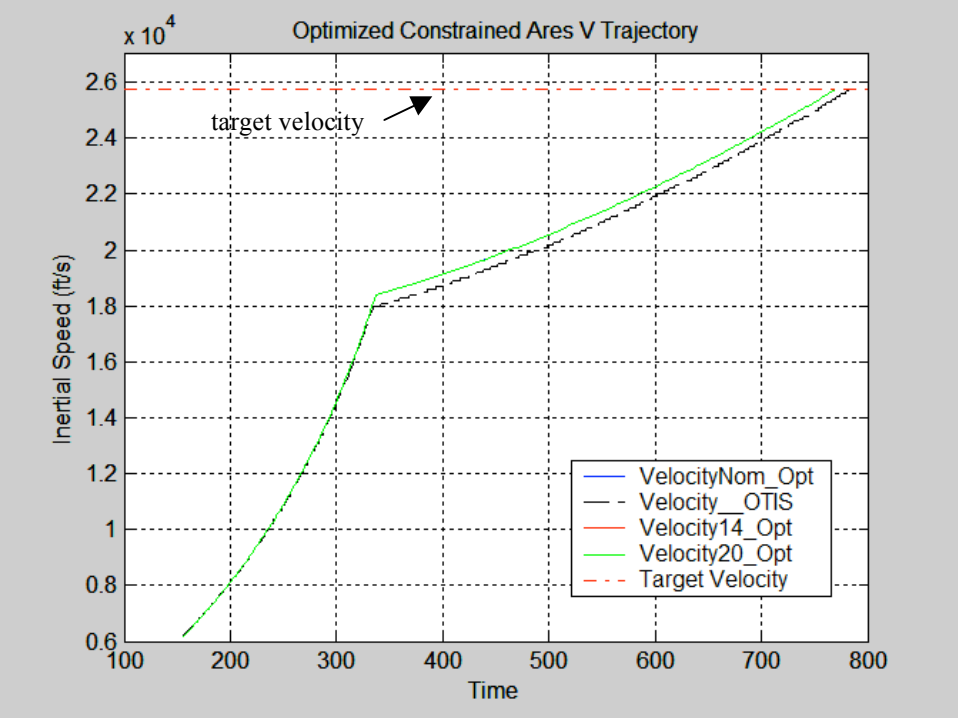

Figure 4.10: Plot of optimal inertial velocity for all test cases with OTIS comparison.

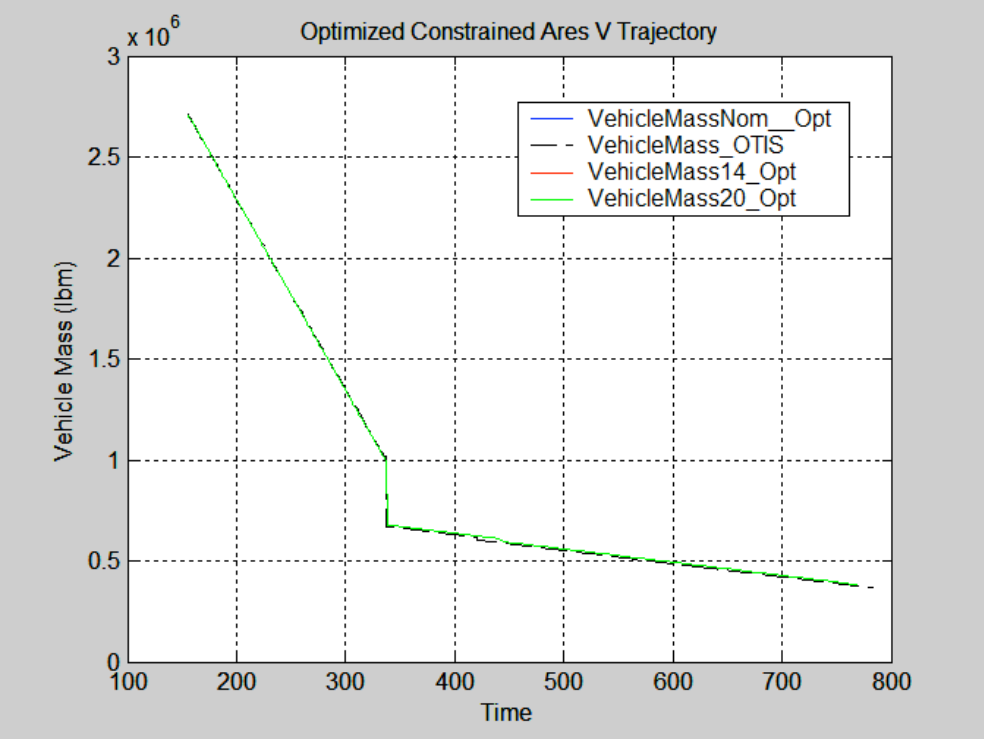

Figure 4.11: Plot of optimal vehicle mass for all test cases with OTIS comparison.

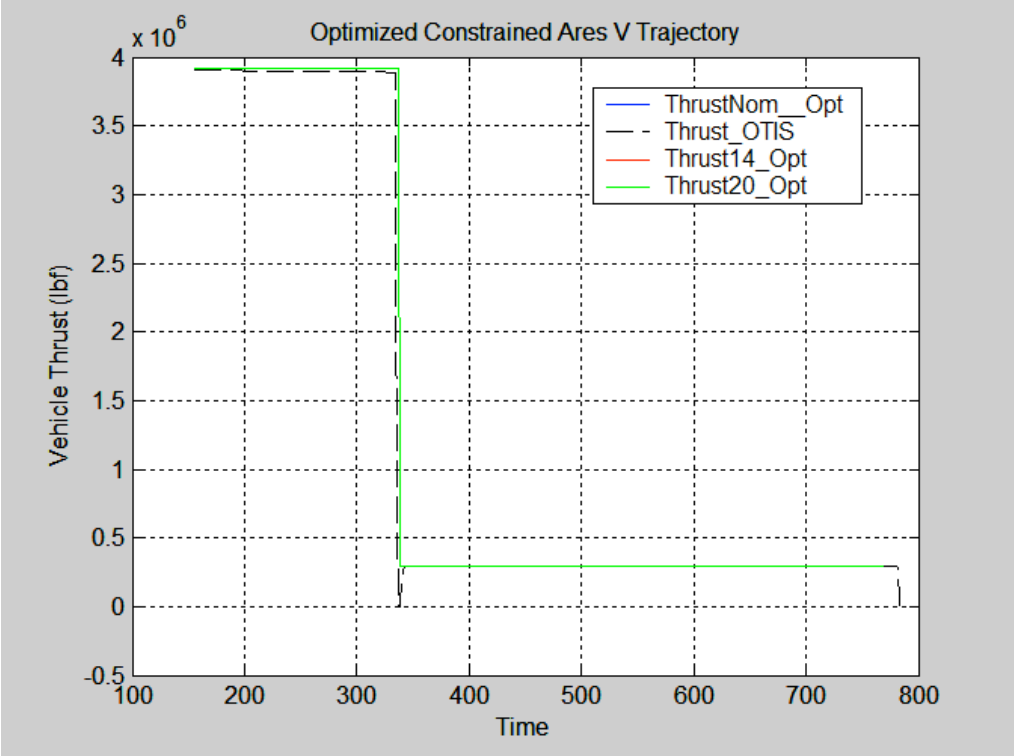

Figure 4.12: Plot of vehicle thrust for all test cases with OTIS comparison.

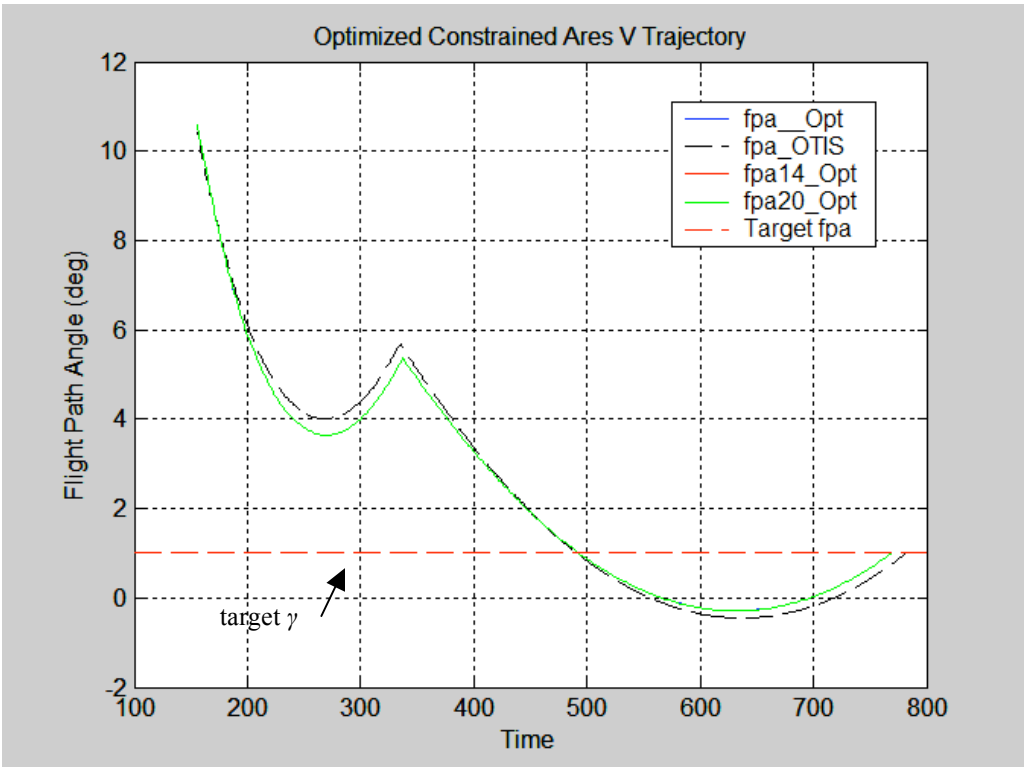

Figure 4.13: Plot of optimal flight path angle for all test cases with OTIS comparison.

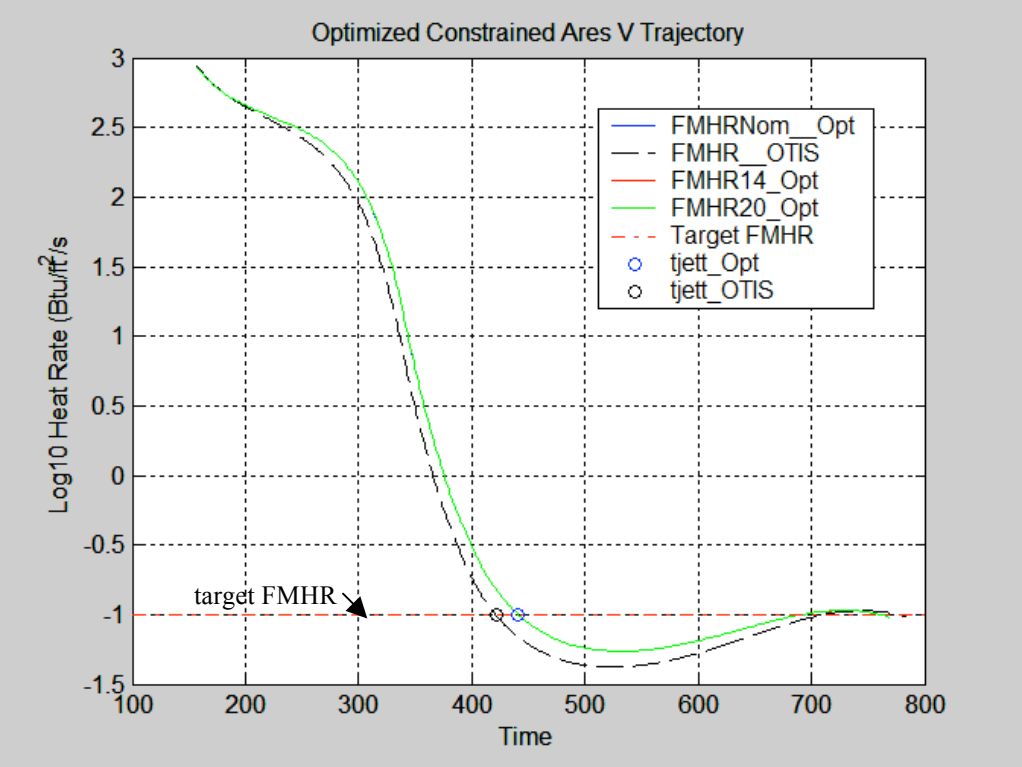

Figure 4.14: Plot of Free Molecular Heat Rate (FMHR) for all test cases with OTIS comparison and jettison times denoted.

The two test cases are essentially identical to the nominal solutions, where all three cases follow the same trajectory. This implies that the linear steering assumption holds and the ascent trajectory solutions are in fact optimal.

4.2.3 Analytical Costate Jump Condition

The optimization routine was unable to converge for the analytical solution derived in Chapter 3. The formulation of the analytical jump condition in Eq. (3.50) should determine the new position costate after payload fairing jettison evaluated with Eq. (3.51), where the optimization routing uses the steering parameter/costate relationships:

$$\overline{A} \cong \dot{\overline{\lambda}}_{V0} = -\overline{\lambda}_{r0} \tag{4.1}$$

$$\overline{B} \cong \overline{\lambda}_{V0} \tag{4.2}$$

Further work may need to be done in order to determine the correct implementation of the analytical jump condition into the optimization routine. The convergence problems may involve the appropriate transformations from linear steering parameters ($\overline{A}$ and $\overline{B}$) to true costates ($\overline{\lambda}_r$ and $\overline{\lambda}_V$). It will be convenient to take advantage of the analytic costate solution so that the complexity of the optimization routine is simplified, reducing the total number of parameters for optimization by eliminating the steering parameter estimates at PLF jettison.

Chapter 5

An Analytic Approach for the Iterative Guidance Design

5.1 Overview

As most guidance algorithms operate under indirect methods, it is useful to develop a solution that can work for on-board guidance algorithms that operate in real-time, as in the Powered Explicit Guidance used for the Shuttle. This chapter presents an analytical solution approach to the control, based on polynomial steering profile and flight-path angle profile assumptions. The analytic solution may then be used as an alternative initial guess for PEG, where a full PEG guidance simulation has been developed in the Simulink environment.

5.2 Powered Explicit Guidance (PEG) Procedure

The Shuttle-based Powered Explicit Guidance, is a guidance scheme consisting of four independent algorithms developed to handle all phases of Shuttle exoatmospheric powered flight. The objective of PEG is to generate steering commands to place the vehicle in a desired position with a desired velocity and with minimal fuel usage [6].

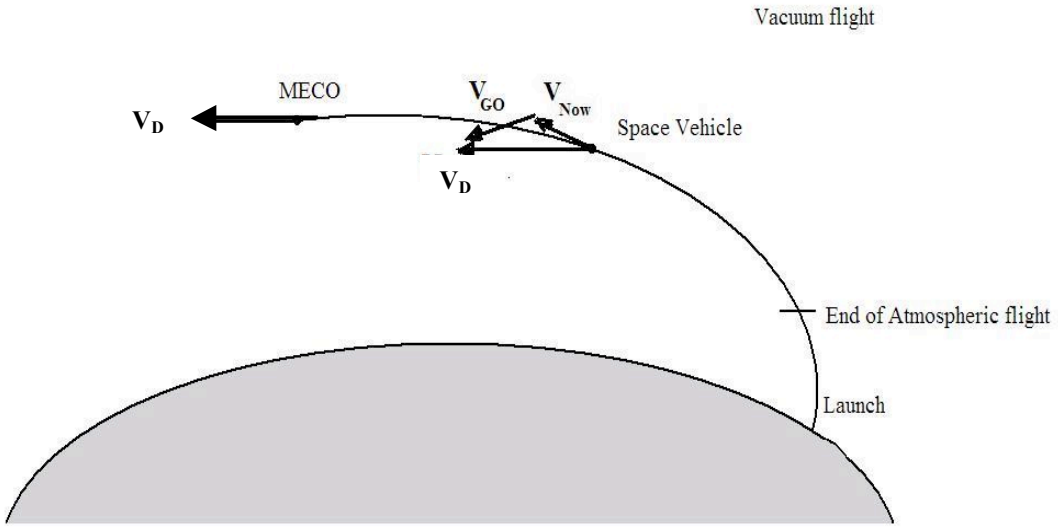

Figure 5.1: PEG ascent guidance to target MECO conditions.

PEG attempts to reach a desired MECO target, as illustrated in Fig. 5.1. The velocity-to-go vector, $\overline{V}_{GO}$, is determined from the difference between the current space vehicle velocity, $\overline{V}_{Now}$, and the desired velocity at MECO, $\overline{V}_D$.

$$\overline{V}_{go} = \overline{V}_D - \overline{V}_{Now} \tag{5.1}$$

PEG updates steering parameters every 1 second (the "guidance cycle") and uses a simplified model of the system dynamics in the predictor step. Full details of the explicit solutions to PEG can be found in Ref. 23, and are summarized in Appendix A.

5.3 Analytic Solutions to the Ascent Guidance Problem

The analytical solution for the control is derived from polynomial assumptions for the ascent trajectory steering profiles. More precisely, the pitch angle (θ) can be shown to follow linear tangent steering and polynomial profiles can also be assumed for the flight

path angle (γ), measured from the horizon to the velocity vector, and the steering angle (α), the angle measured from the velocity vector ($\overline{V}$) to the projection of the vehicle thrust.

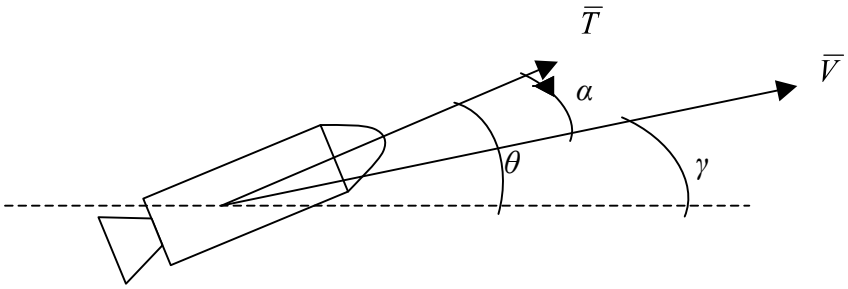

Figure 5.2: Orientation of pitch, steering, and flight path angles.

Following the angle orientations depicted in Fig. 5.2, the steering angle has a direct relationship to both the pitch and flight path angles:

$$\alpha = \theta - \gamma \tag{5.2}$$

Recall that the thrust-steering is discontinuous at the jettison event, thus the linear steering assumption forms two controls: 1) the control vector from start of simulation to PLF jettison, and 2) the control vector from PLF to MECO conditions. Therefore, the analytical solution can also be broken into two parts, corresponding to the same start and terminal events. The remainder of this chapter examines the relevant steering profiles from the off-line optimized solutions (θ, γ, α). From these profiles, the analytic solutions are developed by substituting polynomials that approximate the optimal solutions, allowing the states to be determined analytically.

5.3.1 Analytic Solution: Part One

This section will present the analytic solution from simulation initialization to PLF jettison. The analytic solutions can be derived from the polynomial steering profile assumptions and the ascent equations of motion. Recall from Eq. (2.1):

$$\begin{aligned} \dot{\bar{r}} &= \bar{V} \\ \dot{\bar{V}} &= \bar{g} + \frac{T}{m}\hat{u}_T \end{aligned} \tag{5.3}$$

which can also be expressed using scalar equations:

$$\dot{r} = V\sin\gamma \tag{5.4}$$

$$\dot{V} = a_T\cos\alpha - g\sin\gamma \tag{5.5}$$

$$\dot{\gamma} = \frac{a_T}{V}\sin\alpha - \frac{g}{V}\cos\gamma + \frac{V}{r}\cos\gamma \tag{5.6}$$

where the thrust acceleration (a_T) can also be defined as a function of the exhaust velocity (V_{ex}) and a time constant $\tau = m_0 / \dot{m}$:

$$a_T = \frac{T}{m} = \frac{T}{m_0 - \dot{m}t} = \frac{T/\dot{m}}{m_0/\dot{m} - t} = \frac{V_{ex}}{\tau - t} \tag{5.7}$$

In order to solve the equations of motion [Eqs. (5.4) – (5.6)] analytically, it will be convenient to rewrite the sinγ and cosα terms as polynomials.

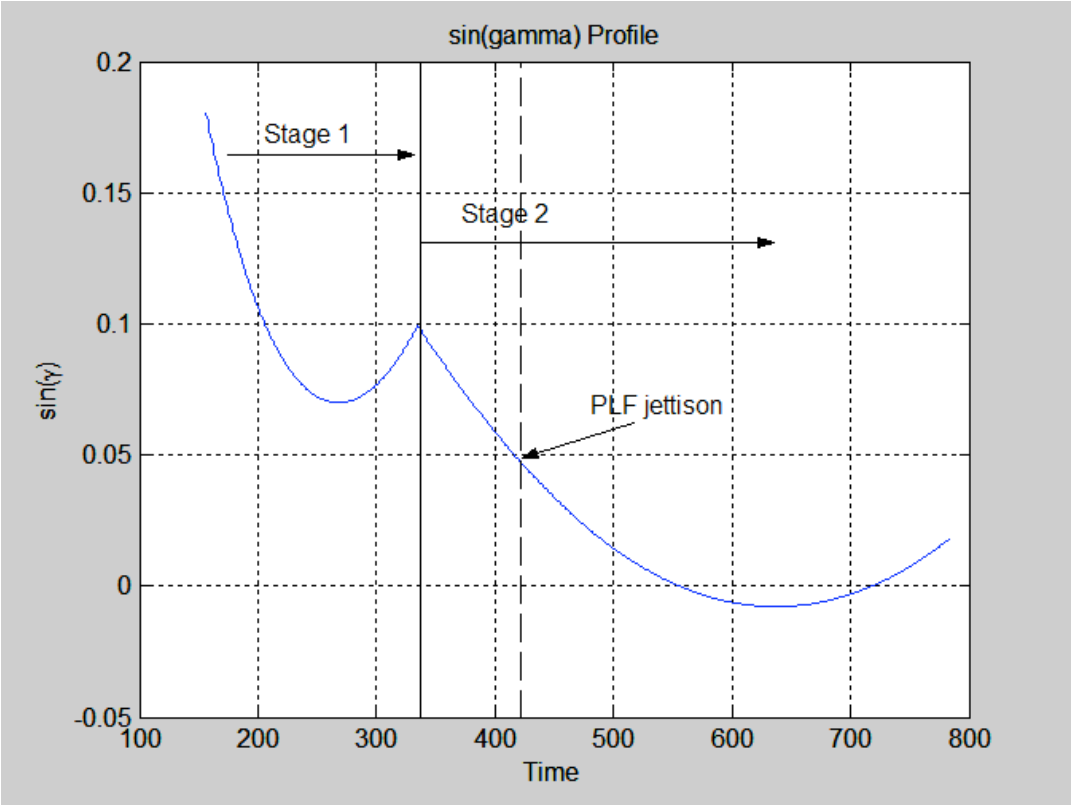

Figure 5.3: Profile for the sine of the flight path angle from the optimized solutions.

The profile shown in Fig. 5.3 illustrates the sine of the flight path angle, resulting from the off-line optimal ascent trajectory. It is obvious that the sinγ profile will assume two polynomial approximations, a quadratic polynomial from start of simulation to the staging point, and a linear polynomial from the staging point to PLF jettison:

$$\sin\gamma = b_2 t^2 + b_1 t + b_0 \qquad \text{stage 1} \qquad (5.8)$$

$$\sin\gamma = b_1 t + b_0 \qquad \text{stage 2 to PLF} \qquad (5.9)$$

The unknown quadratic coefficients in Eq. (5.8) can be determined by solving at initial time t_0

$$b_0 = \sin\gamma_0 \qquad (5.10)$$

and differentiating Eq. (5.8) with respect to time t_0:

$$\frac{d}{dt}(\sin\gamma) = \dot{\gamma}\cos\gamma_0 = b_2 t_0 + b_1 \tag{5.11}$$

where Eq. (5.6) may be substituted with the initial steering angles, α_0 and γ_0. Then

$$b_1 = \dot{\gamma}_0 \cos\gamma_0 \tag{5.12}$$

and b_2 can be determined by solving Eq. (5.8) and substituting the fixed stage 1 burn time (t_1) and corresponding flight-path angle at the staging point (γ_{stage1}). Similarly, the linear polynomial coefficients in Eq. (5.9) are determined by substituting the appropriate times and flight-path angles, such that:

$$b_0 = \sin\gamma_{stage1} \tag{5.13}$$

$$b_1 = \frac{\sin\gamma_{PLF} - b_0}{T_{go}} \tag{5.14}$$

where T_{go} is the free burn time from the staging point to the PLF jettison event.

To determine the analytic relationship for the cosα term, recall the steering relationship from Eq. (5.2). Then applying trigonometric relations:

$$\cos\alpha = \cos(\theta - \gamma) = \cos\theta\cos\gamma - \sin\theta\sin\gamma \tag{5.15}$$

Pitch steering (θ) follows linear tangent steering [5]:

$$\tan\theta = a_1 t + a_0 \tag{5.16}$$

and is derived from the two-dimensional (planar) optimal control problem. Linear steering in combination with the quadratic sinγ profile determines that the cosα profile may also be approximated with a quadratic polynomial for the burn from start of simulation to the staging point:

$$\cos\alpha = c_2 t^2 + c_1 t + c_0 \qquad \text{stage 1} \tag{5.17}$$

Likewise, linear steering in combination with the linear sinγ profile results in a linear cosα profile:

$$\cos\alpha = c_1 t + c_0 \qquad \text{stage 2 to PLF} \qquad (5.18)$$

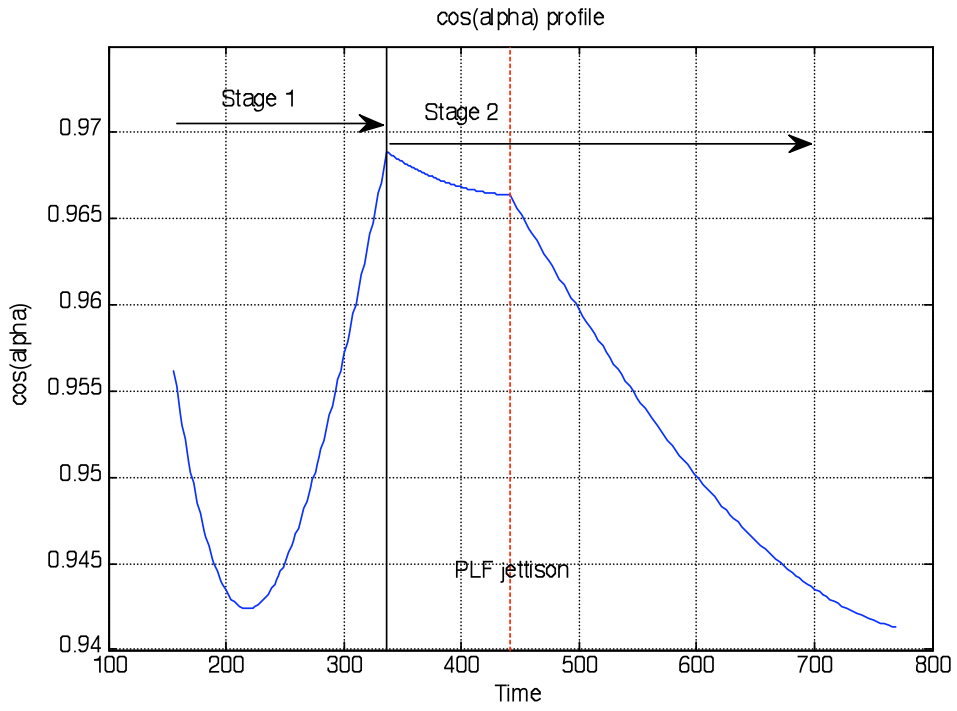

Figure 5.4: Profile of the cosine of the steering angle, α, from the optimized solution.

The quadratic and linear polynomial approximations are verified by the profile shown in Fig. 5.4. Substituting Eqs. (5.8), (5.9), (5.17), and (5.18) into Eq. (5.5), and assuming gravity (g) is a constant determined from the inverse-square relation:

$$\begin{aligned} \int_0^{t_{stage1}} \dot{V} dt = dV = V_f - V_0 &= \int_0^{t_{stage1}} a_{T1} \cos\alpha dt - g \int_0^{t_{stage1}} \sin\gamma dt \\ &= \int_0^{t_{stage1}} \frac{V_{ex1}}{\tau_1 - t} \left(c_2 t^2 + c_1 t + c_0\right) dt - g \int_0^{t_{stage1}} \left(b_2 t^2 + b_1 t + b_0\right) dt \end{aligned} \qquad (5.19)$$

where a_{T1}, V_{ex1}, and τ_1, are the vehicle constants for stage 1, and t_{stage1} refers to the fixed burn time for stage 1. Equation (5.19) results in an analytic integral for the velocity from start to staging:

$$V_f - V_0 = -V_{ex1}\left\{\frac{1}{2}c_2t^2 + c_1t + t\tau_1c_2 + \ln(-\tau_1 + t)\left[c_0 + \tau_1c_1 + \tau_1^2c_2\right]\right\} - g\left(\frac{1}{3}b_2t^3 + \frac{1}{2}b_1t^2 + b_0t\right)\Bigg]_0^{t_{stage1}} \tag{5.20}$$

Applying similar substitutions for the linear polynomial approximations, the analytic velocity integral from staging to PLF is:

$$V_f - V_0 = -V_{ex2}\left\{c_1t + \ln(-\tau_2 + t)\left[c_0 + \tau_2c_1\right]\right\} - g\left(\frac{1}{2}b_1t^2 + b_0t\right)\Bigg]_{t_{stage1}}^{T_{go}} \tag{5.21}$$

where V_{ex2}, and τ_2, are the vehicle constants for stage 2. The integrals for the position:

$$\int_0^{t_{stage1}} \dot{r}dt = r_f - r_0 = \int_0^{t_{stage1}} V\sin\gamma dt \tag{5.22}$$

are determined by substituting the quadratic (or linear) sinγ polynomial. The velocity term now assumes a quadratic (or linear) solution of Eq. (5.20) [or Eq. (5.21)]:

$$V = v_2t^2 + v_1t + v_0 \tag{5.23}$$

$$V = v_1t + v_0 \tag{5.24}$$

Substituting Eq. (5.23) into Eq. (5.22) results in the integral solution for position from start until staging:

$$r_f - r_0 = \frac{1}{5}v_2b_2t^5 + \frac{1}{4}(v_1b_2 + v_2b_1)t^4 + \frac{1}{3}(v_0b_2 + v_1b_1 + v_2b_0)t^3 + \frac{1}{2}(v_0b_1 + v_1b_0)t^2 + v_0b_0t\Bigg]_0^{t_{stage1}} \tag{5.25}$$

while substituting Eq. (5.24) results in the integral solution for position from staging until PLF jettison:

$$r_f - r_0 = \frac{1}{3}v_1 b_1 t^3 + \frac{1}{2}(v_0 b_1 + v_1 b_0)t^2 + v_0 b_0 t \Big]_0^{t_{stage1}} \tag{5.26}$$

Notice that there needs to be knowledge of the initial flight path angle (γ_0) and its derivative ($\dot{\gamma}_0$) in order to solve Eqs. (5.8)-(5.14). The initial flight path angle is known from the set initial conditions (r_0 and V_0) and $\dot{\gamma}_0$ may be determined from Eq. (5.6) if an initial estimate of α_0 (or θ_0) is made. The additional free parameters needed to evaluate the analytic solutions include the position and velocity at the staging point (r_{stage1} and V_{stage1}), the burn time from staging to the PLF jettison event (T_{go}), and the pitch angle at PLF jettison (θ_{PLF}). The target conditions (r_{PLF} and V_{PLF}) for the analytic solutions to part one of the ascent trajectory are fixed due the heat-rate constraint at PLF jettison, such that meeting the target states at PLF jettison meets the heat-rate constraint from Eq. (2.2).

5.3.2 Analytic Solution: Part Two

The second part of the analytic solution pertains to the trajectory from PLF jettison to MECO conditions. Refer to Fig. 5.3, which shows that for the second solution, only one quadratic polynomial approximation is required for the sinγ profile, and subsequently, only one quadratic polynomial approximation is required for the cosα profile. The corresponding analytic solution for the velocity is:

$$V_f - V_0 = -V_{ex2}\left\{\frac{1}{2}c_2 t^2 + c_1 t + t\tau_1 c_2 + \ln(-\tau_2 + t)\left[c_0 + \tau_2 c_1 + \tau_2^2 c_2\right]\right\} - g\left(\frac{1}{3}b_2 t^3 + \frac{1}{2}b_1 t^2 + b_0 t\right)\Big]_0^{T_{go}} \tag{5.27}$$

where T_{go} is the unknown burn time from PLF jettison to target conditions. The integral solution for the position is:

$$r_f - r_0 = \frac{1}{5}v_2 b_2 t^5 + \frac{1}{4}(v_1 b_2 + v_2 b_1)t^4 + \frac{1}{3}(v_0 b_2 + v_1 b_1 + v_2 b_0)t^3 + \frac{1}{2}(v_0 b_1 + v_1 b_0)t^2 + v_0 b_0 t\Big]_0^{T_{go}} \tag{5.28}$$

The parameters needed to solve the analytic solutions for part one that have been developed in this chapter are presented in Table 5.1.

Table 5.1: Summarization of parameters for analytic solutions to part one of the ascent trajectory.

Part One: Start of Simulation to PLF Jettison		
Event	**Parameter**	**Condition**
Start of burn	position, r_0	known
Start of burn	velocity, V_0	known
Start of burn	flight path angle, γ_0	known
Start of burn	steering angle, θ_0 (or α_0)	free
Staging point	position, r_{stage1}	free
Staging point	velocity, V_{stage1}	free
Staging point	flight path angle, γ_{stage1}	free
Staging point	burn time for stage 1, t_{stage1}	known
Target Conditions	position, r_{PLF}	known
Target Conditions	velocity, V_{PLF}	known
Target Conditions	flight path angle, γ_{PLF}	known
Target Conditions	steering angle, θ_{PLF} (or α_{PLF})	free
Target Conditions	T_{go}	free

The parameters needed to solve the analytic solutions for part two are presented in Table 5.2.

Table 5.2: Summarization of parameters for analytic solutions to part two of the ascent trajectory.

Part Two: PLF Jettison to MECO		
Event	**Parameter**	**Condition**
Start of burn	position, r_{PLF}	known
Start of burn	velocity, V_{PLF}	known
Start of burn	flight path angle, γ_{PLF}	known
Start of burn	steering angle, θ_{PLF}	free
Target Conditions	position, r_f	known
Target Conditions	velocity, V_f	known
Target Conditions	flight path angle, γ_f	known
Target Conditions	T_{go}	free

The polynomial relationships and analytical solutions for position and velocity aid in reducing the number of free parameters listed in Tables 5.1 and 5.2. The analytic solution for part one requires only three of the free parameters listed in Table 5.1: γ_{stage1}, θ_{PLF}, and T_{go}, where T_{go} is the burn time from the staging point to the PLF jettison. The initial sinγ coefficients in Eqs. (5.8) may be determined by assuming at least one of the initial steering angles, either θ_0 or α_0, which allows for the remaining relationships in Eqs. (5.9)-(5.14) to be solved. Table 5.2 indicates that there are two free parameters needed to evaluate the analytic solutions for part two. The initial guess for T_{go}, that is, the burn time from PLF jettison to MECO conditions, can be approximated by the impulsive solution:

$$T_{go} = \tau\left(1 - \exp\left(-\Delta V / V_{ex}\right)\right) \tag{5.29}$$

where the ideal impulsive change in velocity is the difference between the desired speed and initial speed, $\Delta V = V_D - V_0$. Thus, the analytic solutions for part two are dependent on only one initial guess for the unknown initial pitch angle, θ_{PLF}. For both the analytic solutions to part one and part two, boundary conditions, where appropriate (desired initial and final steering angles and desired initial and final positions and velocities) were extracted from the off-line optimized ascent trajectory solutions.

5.3.3 Iterative Updating Procedure

After making initial guesses for the appropriate unknown parameters, the analytic relationships, defined in the previous section, determine the projected ascent trajectory. The parameters are updated through an iterative procedure that corrects the errors in the

projected and desired position and velocity, (r_{end}, V_{end}) and (r_D, V_D), respectively. For the analytic solution to part one, the iterative procedure first attempts to find the correct T_{go} through a linear search based on the velocity errors:

$$T_{go} = T_{go} + \frac{dt}{dV} V_{error} \tag{5.30}$$

where dt/dV is the inverse of Eq. (5.4) and $V_{error}=V_D - V_{end}$. The remaining two parameters are updated by using the position error, but there is only one condition to update two parameters. This issue is resolved by using the pseudoinverse of a matrix, which performs the matrix inverse of a non-square matrix. Then the parameter updates (δu) based on the position error (δr) becomes:

$$\delta\overline{u} = \begin{bmatrix} \delta\theta_{PLF} \\ \delta\gamma_{stage1} \end{bmatrix} = \alpha_s \, pinv(M)\delta r \tag{5.31}$$

where $\alpha_s \leq 1$ is a scaling factor that adjusts the search direction, and M is the matrix of partials that is constructed by making small changes in the parameters and 'shooting' perturbed trajectories so that the partials are finite differences:

$$[M] = \begin{bmatrix} \partial r / \partial\theta & \partial r / \partial\gamma \end{bmatrix} \cong \begin{bmatrix} \Delta r / \Delta\theta & \Delta r / \Delta\gamma \end{bmatrix} \tag{5.32}$$

The pseudoinverse finds the solution that minimizes $\delta\overline{u}^T \delta\overline{u}$. Then the parameter updates are:

$$\begin{aligned} \theta_{PLF} &= \theta_{PLF} + \delta\theta_{PLF} \\ \gamma_{stage1} &= \gamma_{stage1} + \delta\gamma_{stage1} \end{aligned} \tag{5.33}$$

The iterative procedure for the analytic solutions to part two follows a similar updating procedure, where the T_{go} estimate (time from PLF to MECO) is updated using the

velocity errors and the initial guess for the pitch angle at PLF jettison, θ_{PLF}, is updated using the resulting position errors.

5.3.4 Applying the Analytic Solutions to PEG

PEG solves the two-point boundary-value problem for vacuum flight through an iterative process with fixed initial conditions. The routine initializes the controls:

$$\begin{aligned} \left\| \dot{\bar{\lambda}}_V \right\| &= 10^{-5} \\ \bar{\lambda}_V &= \frac{\bar{V}_0}{\left\| \bar{V}_0 \right\|} \end{aligned} \tag{5.34}$$

and uses the impulsive solution for the initial ΔV. Then the velocity to be gained by thrust is:

$$\bar{V}_{go} = \Delta V \frac{\bar{V}_0}{\left\| \bar{V}_0 \right\|} = \Delta V \bar{\lambda}_{V0} \tag{5.35}$$

where ΔV is just a scalar. Therefore, the analytic solutions developed thus far, can serve as an alternative initialization for PEG, where the scalar ΔV's from the analytic solutions can be used to determine $\bar{V}_{go}$.

Chapter 6

Results of the Analytic Solution Method

6.1 Overview

This chapter examines the analytical solution approach to the optimal control problem, substituting polynomial approximations for the steering profiles. The solutions to the analytic approach were applied to PEG, the Shuttle-based guidance routine, modeled in Simulink, where the alternative initialization provided by the analytic solutions proved to be useful for convergence of the vacuum flight problem.

6.2 Results of the Analytic Solutions: Part One

The analytical solution method described in Chapter 5 has been formulated into an iterative routine that updates initial guesses on steering angles (θ and γ) and time-to-go (T_{go}) by correcting the errors in both position and velocity. Initial results of the ascent trajectory showed significantly large errors in the projected position, leading to the presumption that there were issues with the inherent polynomial approximations for sinγ and cosα. To adjust these errors, it was decided that the projected position should be calculated using trapezoidal integration, instead of assuming a quadratic (or linear) profile for the velocity (V) as in Eq. (5.25). The trade-off for this adjustment is the introduction of a numerical integral into the analytic solutions. The solutions, however, show a more similar convergence to the optimal values with this numerical adjustment.

The optimal trajectory solutions obtained through off-line direct parameter optimization will serve as the basis for the desired values of the unknown parameters, previously denoted in Chapter 5. Based on these solutions, the initial guesses for the

unknown parameters were chosen close to the optimal values in order to provide a faster convergence rate for testing purposes. An initial angle (θ_0) was assumed to be 27 deg, where the remaining unknown parameters are summarized in Table 6.1.

Table 6.1: Initial guesses for analytical solutions.

Parameter	Value	Optimal
Solution Part One		
θ_{PLF}	17 deg	17.03 deg
γ_{stage1}	5 deg	5.37 deg
T_{go}	100 sec	103.87 sec
Solution Part Two		
θ_{PLF}	17 deg	17.03 deg

The more complicated analytic solution for part one makes up the more interesting set of results, and will be the bulk of the discussion in this chapter. Using the estimates listed in Table 6.1, the initial analytical results are summarized in Table 6.2.

Table 6.2: Converged parameter values from analytical solutions for part one.

Converged Solutions					
Scalar	*Iterations*	*Integration Steps*	*T_{go}(sec)*	*θ_{PLF} (deg)*	*γ_{stage1}(deg)*
α_s = 1	*247*	*N_1= N_2= 100*	*131.81*	*21.36*	*9.36*

Recall α_s is the scalar that adjusts the search direction of the pseudoinverse. For the solutions to part one, which include quadratic and linear polynomial approximations for both sinγ and cosα, N_1 refers to the number of integration steps taken for the quadratic approximation and N_2 refers to the number of integration steps taken for the linear approximation. The burn time, T_{go}, for the solution to part one, refers to the burn time to the PLF jettison event, relative to the staging point. The converged solutions listed in Table 6.2 all bear a significant difference from the optimal values. Figures 6.1 and 6.2 show the resulting velocity and position profiles from the analytic solutions.

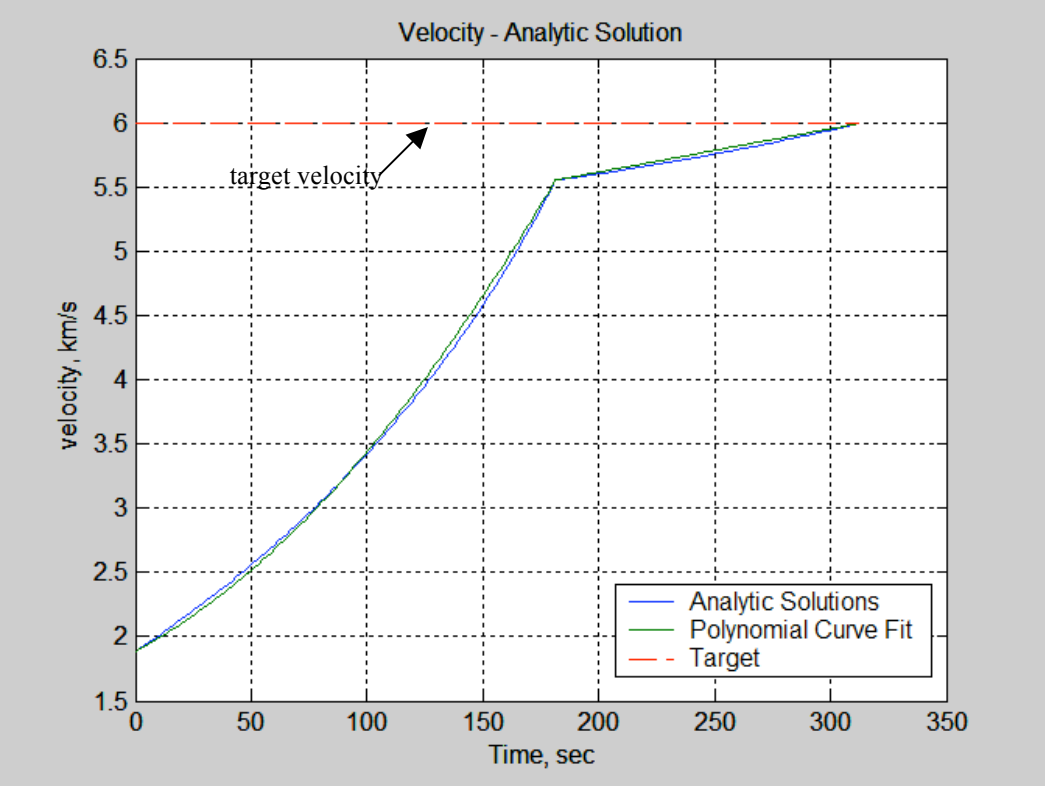

Figure 6.1: Analytical solution for velocity for part one.

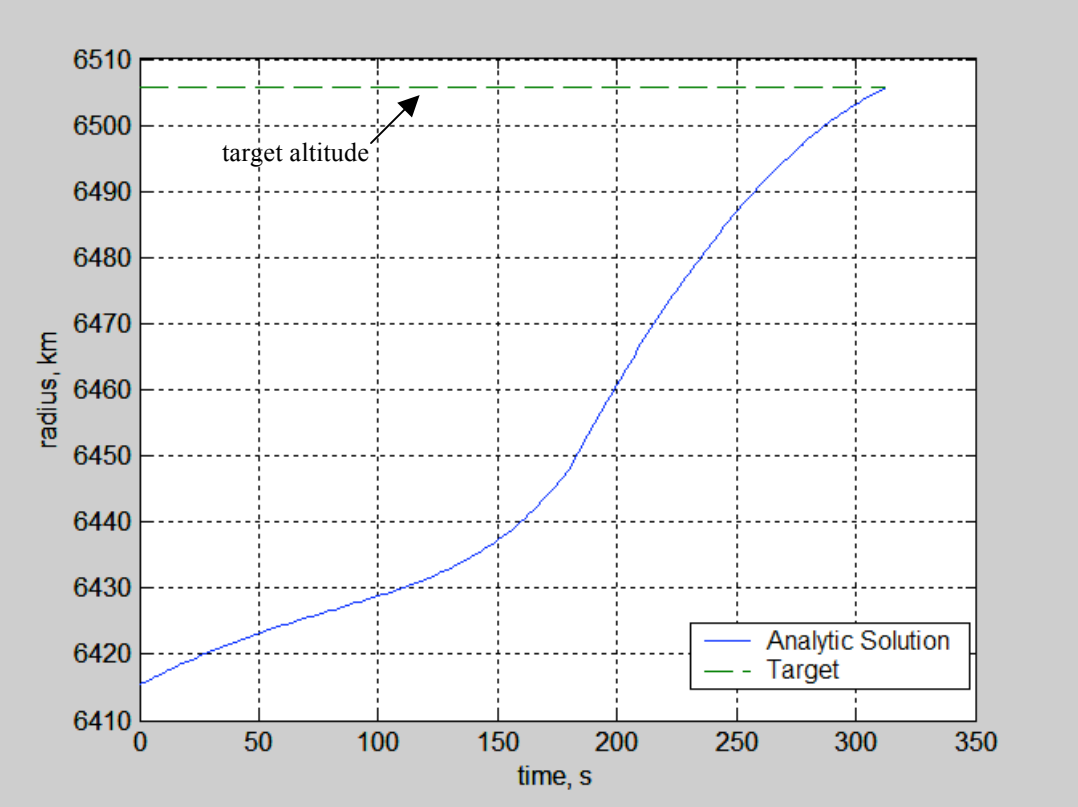

Figure 6.2: Analytical solution for position for part one.

Though the target conditions are reached, the differences in the analytical solution and direct curve fit for the velocity profile in Fig. 6.1 indicate that the converged parameter solutions could benefit from adjustments to the iteration procedure. This includes adjusting the step size of the scalar search direction (α_s) and the number of trapezoidal integration steps, N_1 and N_2. Table 6.3 summarizes just a few variations of these factors and the resulting parameters:

Table 6.3: Converged solutions with variations in iteration parameters.

Converged Solutions						
Case	*Scalar*	*Iterations*	*Integration Steps*	T_{go}*(sec)*	θ_{PLF} *(deg)*	γ_{stage1}*(deg)*
1	$\alpha_s = 1$	*247*	$N_1 = N_2 = 100$	*131.81*	*21.36*	*9.36*
2	$\alpha_s = 1$	*593*	$N_1 = N_2 = 50$	*235.37*	*34.44*	*22.43*
3	$\alpha_s = 1$	*116*	$N_1 = N_2 = 200$	*99.49*	*15.23*	*3.23*
4	$\alpha_s = 1$	*133*	$N_1 = 50, N_2 = 200$	*111.28*	*17.67*	*5.67*
5	$\alpha_s = 0.5$	*494*	$N_1 = N_2 = 100$	*131.86*	*21.36*	*9.36*
6	$\alpha_s = 0.5$	*178*	$N_1 = N_2 = 300$	*90.2*	*13.22*	*1.23*
7	$\alpha_s = 0.25$	*433*	$N_1 = 100\ N_2 = 200$	*106.73*	*16.69*	*4.69*
8	$\alpha_s = 0.25$	*426*	$N_1 = 100\ N_2 = 300$	*97*	*14.71*	*2.72*

The highlighted portions of Table 6.3 were determined to be the combinations of parameters that provided the "best" converged solutions, that is, the converged solutions were close to the desired optimal values. Case 4 produces steering angles close to the optimal values, while Case 7 produces a converged solution for T_{go} that is closer to the optimal jettison time. In either case, the converged solutions provide a "good" initial guess for the full PEG guidance simulation.

6.3 Results of the Analytic Solutions: Part Two

The results of the analytic solutions for part two, that is the solution from PLF to MECO, are summarized in Table 6.4.

Table 6.4: Converged parameter values from analytic solutions to part two.

Converged Solutions			
Iterations	T_{go}*(sec)*	θ_{PLF} *(deg)*	θ_f *(deg)*
5	*336.52*	*17.64*	*20.56*

Figures 6.3 and 6.4 show the resulting position and velocity profiles for the analytic trajectory from PLF to MECO.

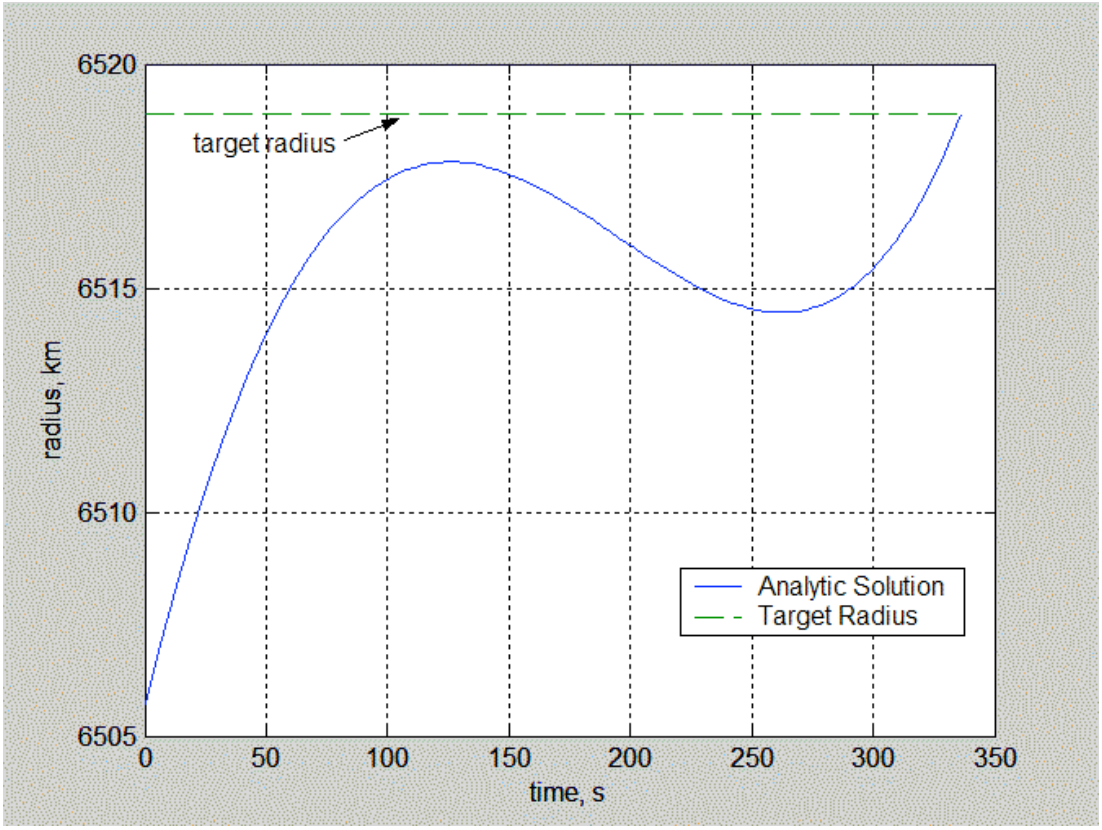

Figure 6.3: Analytic solution for position for part one.

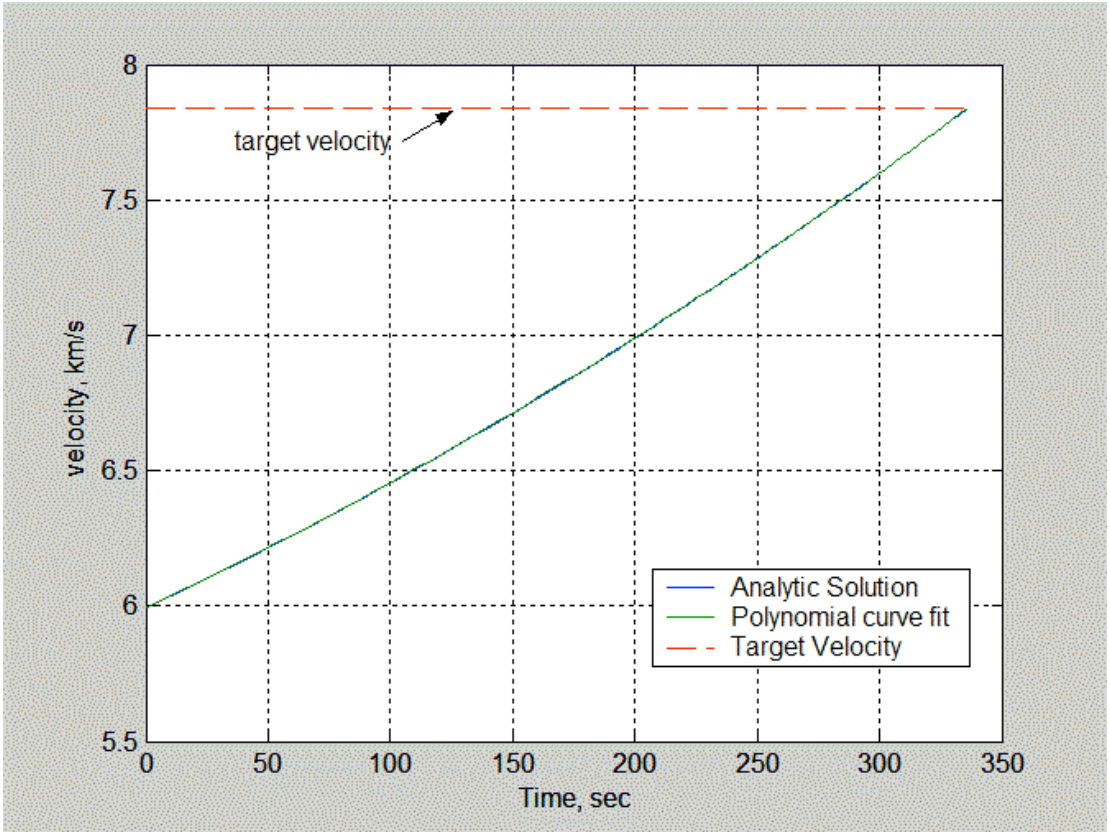

Figure 6.4: Analytic solution for velocity for part two.

The converged solutions are very close to the optimal off-line results, and Fig. 6.4 shows that the analytic solutions follow match well to the polynomial approximation.

The full analytic solution for the ascent trajectory has been plotted in Figs. 6.5 and 6.6. The results of the off-line optimization have also been included for comparison.

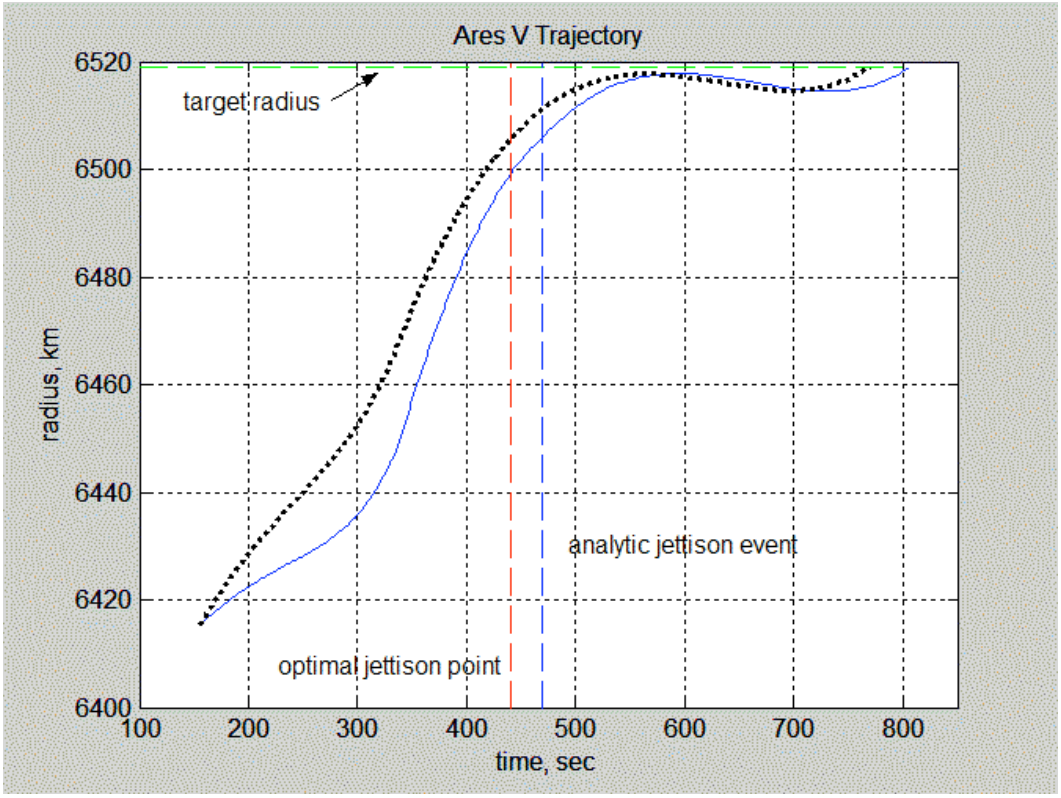

Figure 6.5: Analytic radius vs. optimal radius.

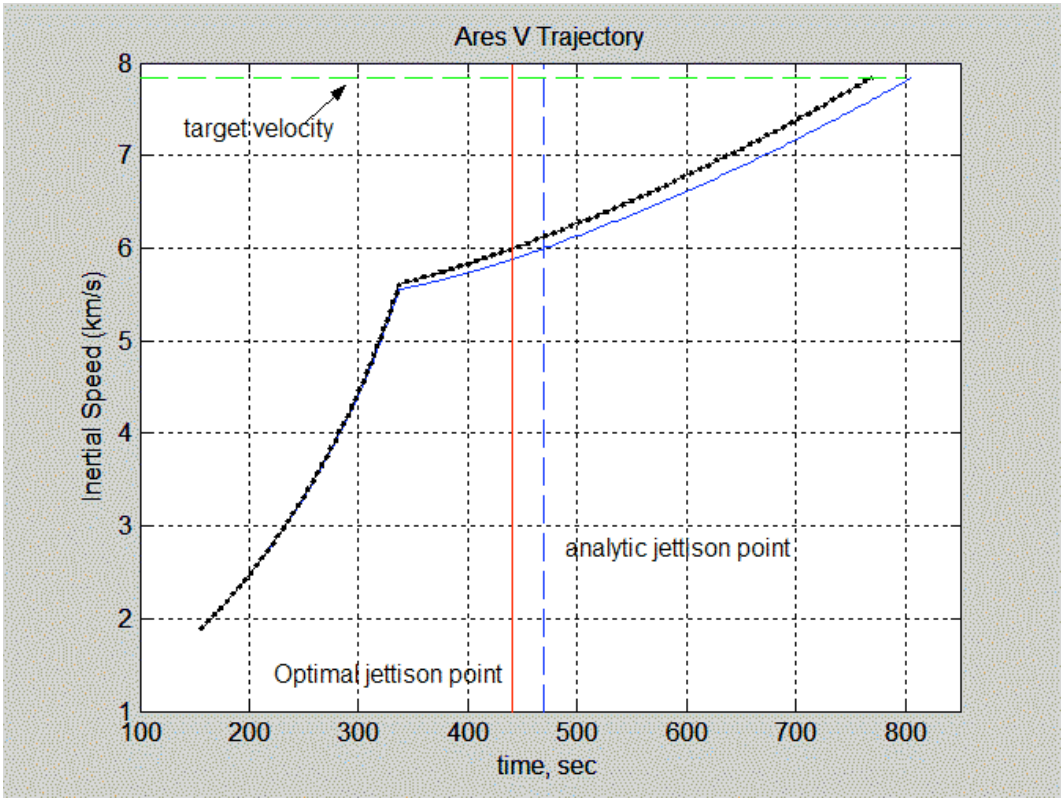

Figure 6.6: Analytic velocity vs. optimal velocity.

The analytic solutions result in a longer flight time, and as indicated on Figs. 6.5 and 6.6, predict a later PLF jettison time than the optimal jettison time. The results of the analytic solutions have been summarized in Table 6.5.

Table 6.5: Summarization of analytic results.

Parameter	Optimization	Analytic
t_{PLF} (s)	441.02	468.93
t_f (s)	769.45	805.46
r_f (km)	6518.89	6518.89
V_f (km/s)	7.84	7.84

Though the analytic solutions did not converge to the optimal values, the idea of producing an analytic result is to provide PEG with an initial "good" guess.

6.4 PEG Solutions

The PEG algorithm, which solves the on-board guidance problem in real-time, has been modeled in Simulink and is shown here for completeness:

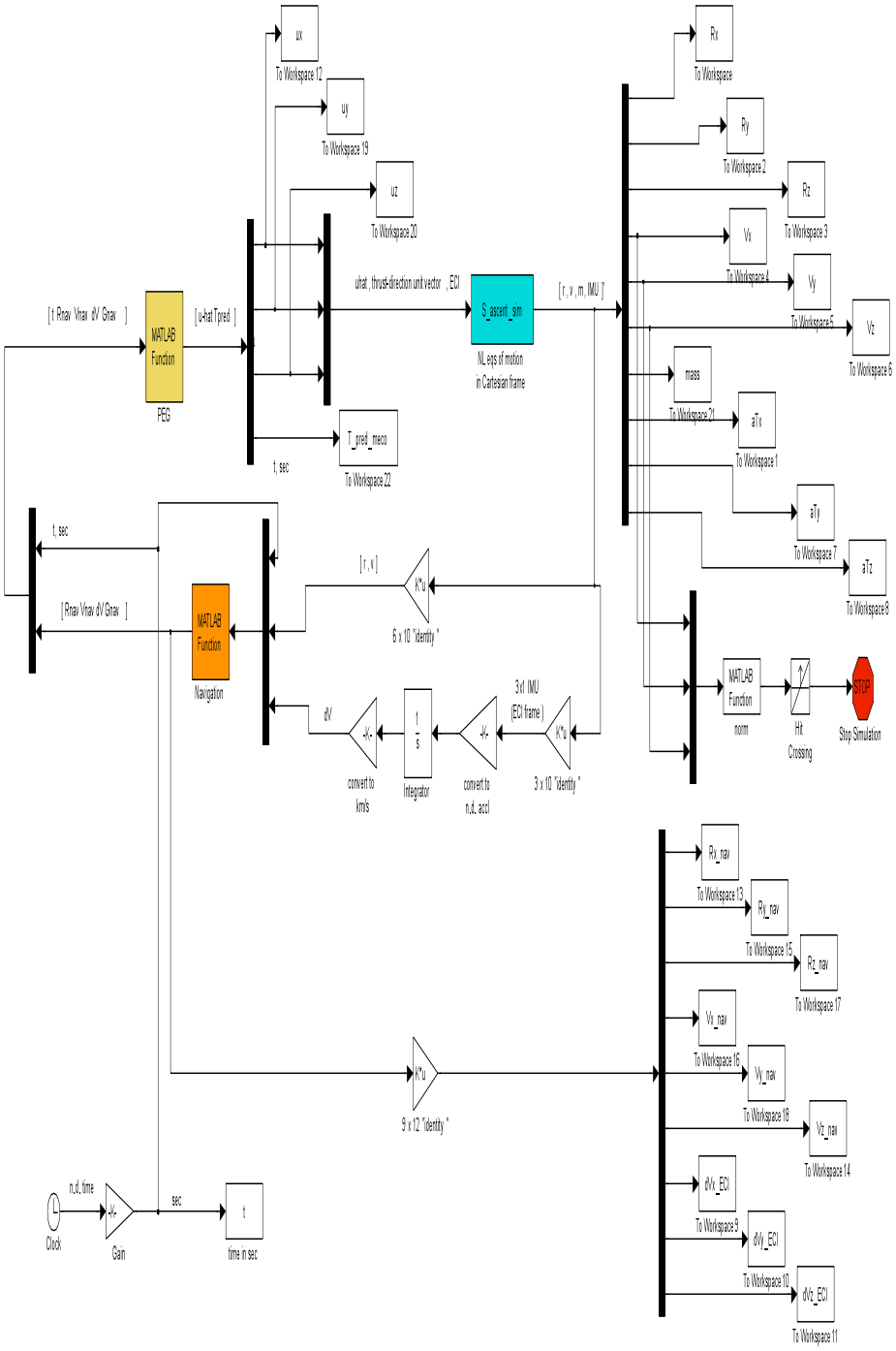

Figure 6.7: Block diagram of PEG modeled in Simulink.

The ascent problem has been divided into three sub-problems:

1. Mode 1: Start of simulation to PLF jettison.
2. Mode 2: Staging point to PLF jettison.
3. Mode 3: PLF jettison to MECO conditions.

where the guidance routine attempts to match the final states to the appropriate target conditions. The first mode should be the most difficult, as it is trying to match a trajectory from the starting point, through the staging event, to the PLF jettison event, where recall the states at PLF jettison are fixed due to the heat-rate constraint imposed at the jettison event.

The first important result to note, is that when PEG self starts with the initialization presented in Section 5.3.4, the PEG routine will not converge on its own. Therefore, recognizing that instead of requiring a thrust vector, the key factor to initialize PEG is to provide a good initial estimate of the ΔV's, the analytic solutions serve as the alternative method to initializing the guidance routine. Then, the scalar ΔV's from the converged analytic solutions are applied to PEG by:

$$\overline{V}_{go} = \Delta V_{analytic} \frac{\overline{V}_{nav}}{\left\| \overline{V}_{nav} \right\|} \tag{6.1}$$

where $\overline{V}_{go}$ is a unit vector aligned with the velocity and $\overline{V}_{nav}$ is the velocity vector evaluated from the navigation guidance pass.

Table 6.6 lists the scalar values of ΔV determined from the converged analytic solutions and can be substituted into Eq. (6.1) to determine the initial estimates of the velocity-to-go for PEG. Table 6.7 summarizes the results of PEG, using the updated version of the initial estimates.

Table 6.6: Scalar values of ΔV as determined by analytic solutions.

Event	ΔV (km/s)
Start to Staging	4.0763
Staging to PLF	0.562
PLF to MECO	1.9707

Table 6.7: Summarization of PEG results.

Parameter	Value
Final mission elapsed time	771 s
Final simulation time	326.9 s
Final position (r) error	5.5 m
Final velocity (V) error	0.2781 m/s
Final flight path angle (γ) error	7.59×10^{-4} deg
final inclination (i) error	-6.62×10^{-8} deg
final mass (m)	172,780 kg

Table 6.8 compares the final values of the jettison time (t_{PLF}), total flight time (t_f), and the final vehicle mass (m_f) from the PEG solutions and the off-line optimal solutions.

Table 6.8: Comparison of PEG simulation results.

Parameter	Optimization	PEG
t_{PLF} (s)	441.02	444.00
t_f (s)	769.45	771.00
m_f (kg)	173,430	172,780

The PEG guidance solutions produce a slightly longer total flight time, exceeding the optimal total flight time by approximately 1.5 seconds. This seemingly small flight time difference, in fact, still impacts the optimal fuel consumption, where the longer PEG solution results in a final mass of 172,780 kg, corresponding to an excess of 650 kg of burned fuel than the optimized solution. Figures 6.8–6.13 illustrate the important trajectory parameters from the converged solutions resulting from PEG, and are compared to the optimal off-line trajectory parameters, previously presented in Chapter 4.

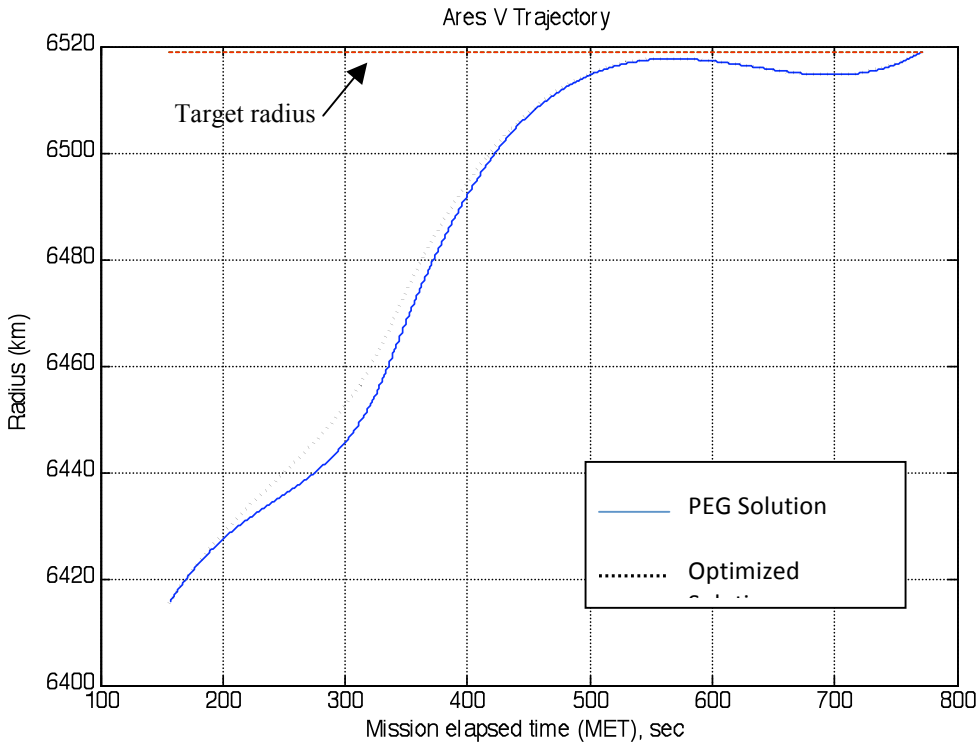

Figure 6.8: Converged solutions for radius of the ascent trajectory.

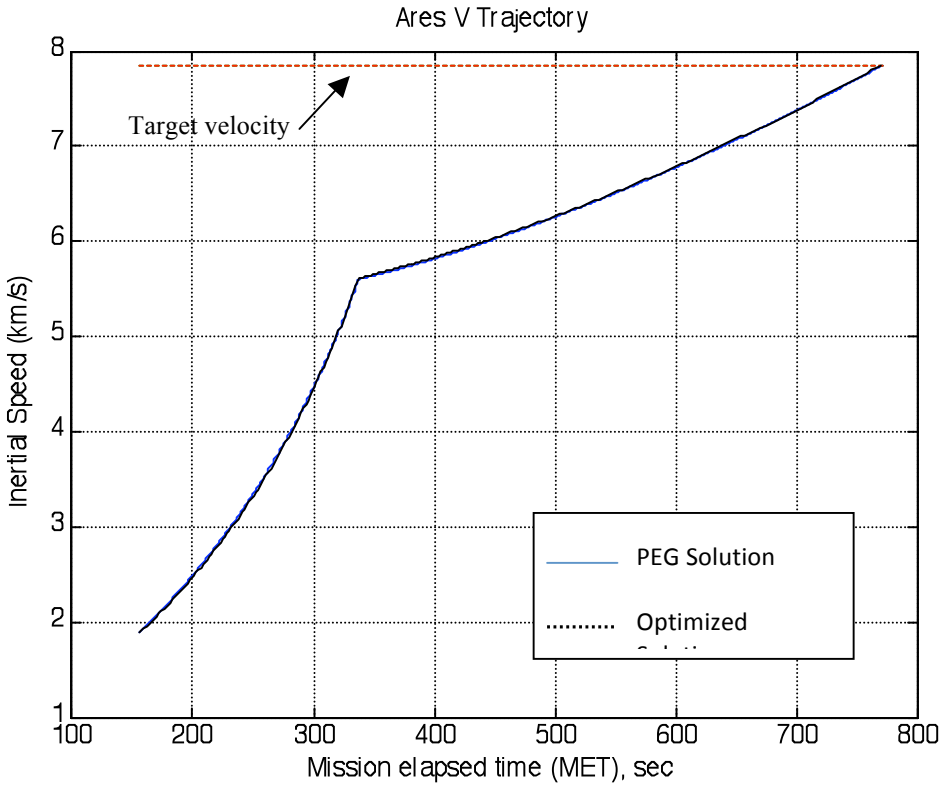

Figure 6.9: Converged solutions for velocity of the ascent trajectory.

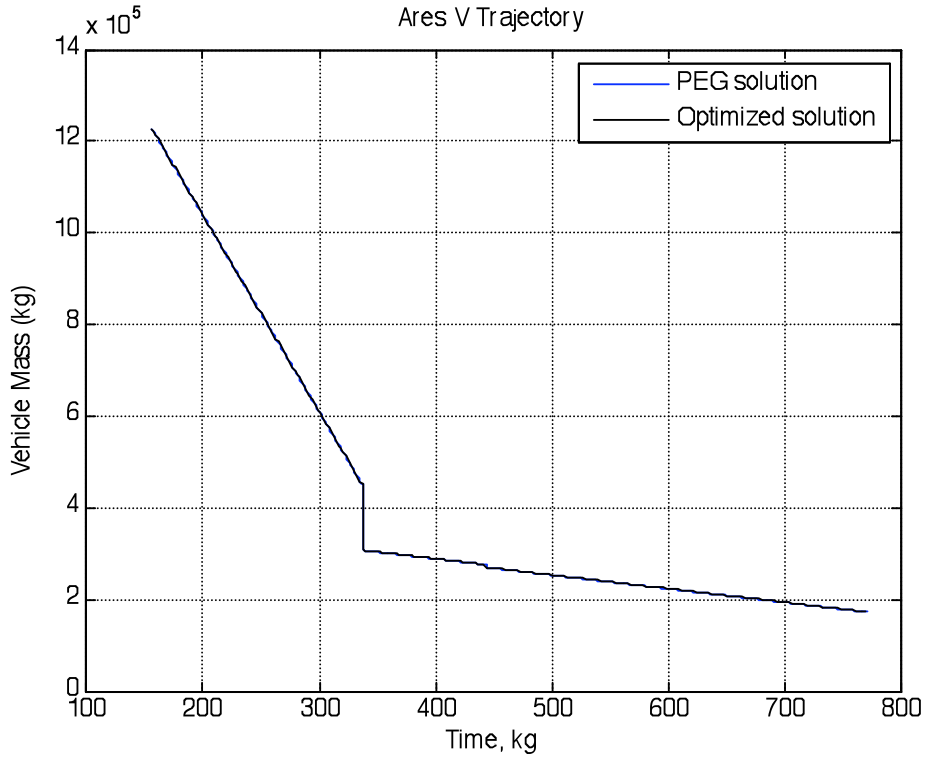

Figure 6.10: Converged solutions for vehicle mass.

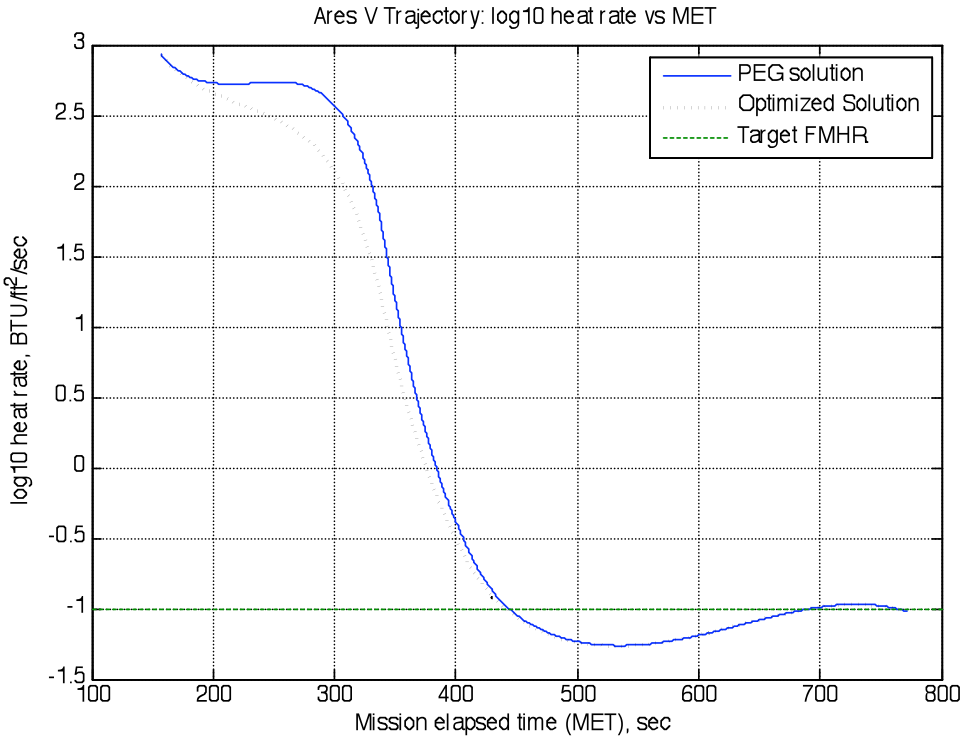

Figure 6.11: Converged solutions for the Free Molecular Heat Rate (FMHR).

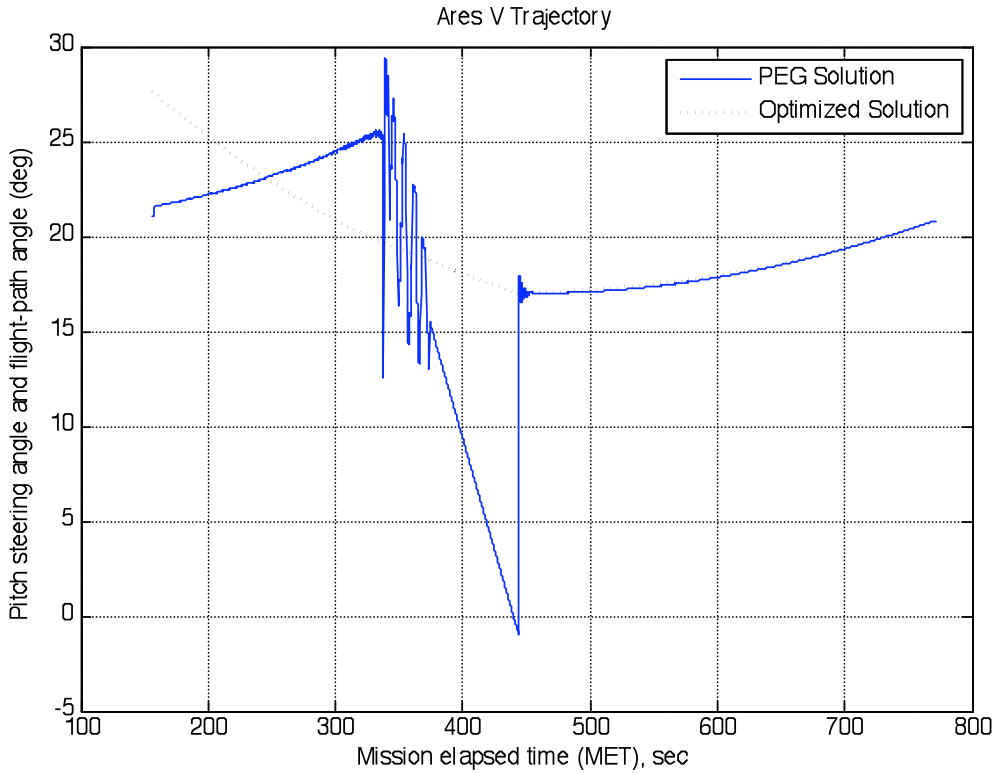

Figure 6.12: Converged solutions for the pitch steering profile.

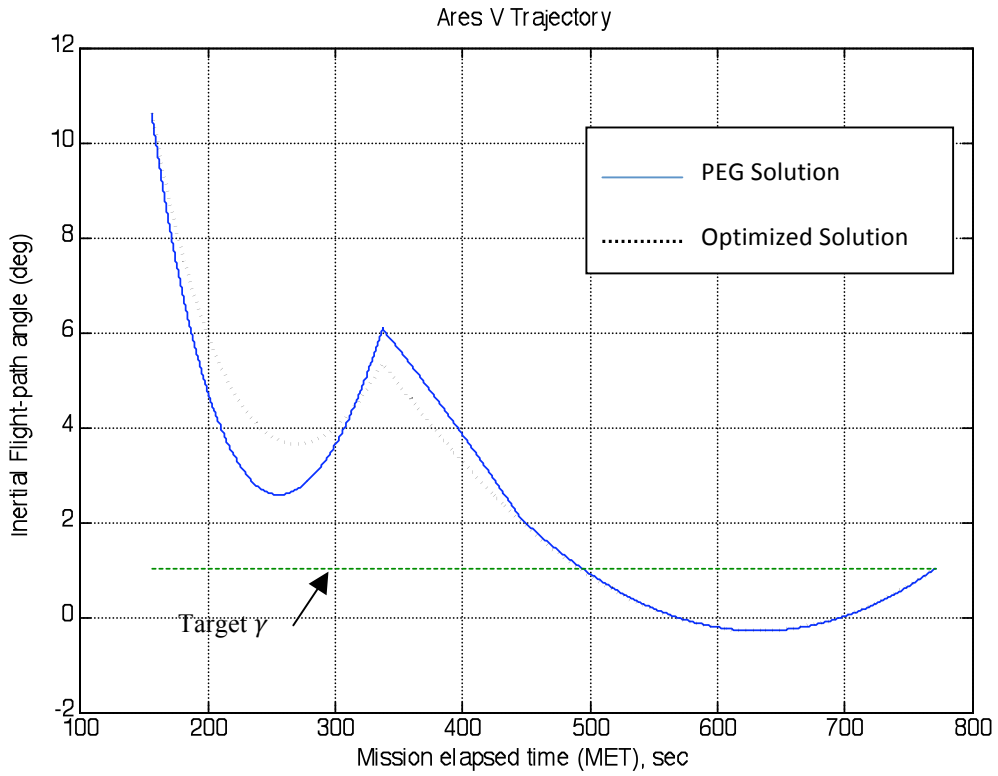

Figure 6.13: Converged solutions for the flight path angle profile.

In general, using the alternative initialization parameters to determine $\overline{V}_{go}$, PEG is able to converge to the desired target conditions. Figure 6.8 shows the ascent radius history for the PEG solution and the optimal solution. Note, PEG deviates from the optimal solution from the start of initialization to the PLF jettison, then seems to match the optimal profile upon reaching the PLF jettison event. Figures 6.9 and 6.10 show that the velocity and vehicle mass solutions match almost identically. The heat-rate constraint history has been plotted in Fig. 6.11, where the trends in the PEG profile and optimal profile are very close. Most importantly, it is evident that the heat-rate constraint which fixes the target states at the PLF jettison point, has been met in the PEG simulations, and the jettison time matches that of the optimal value. The pitch profile in Fig. 6.12 illustrates where PEG may have convergence problems. The pitch steering predicted by PEG is very poor (when compared to the optimal pitch profile) from the start of simulation to the jettison event. Once the PLF jettison event occurs, though, the pitch profile matches the optimal solution. Despite the discrepancy in the PEG pitch profile to the optimal profile, PEG still does a good job of estimating the pitch angle until the staging point. During the burn from the staging point to PLF jettison, PEG is very unstable, until T_{go} is approximately 40-60 seconds, where upon, the guidance routine holds the last solution. This is a standard substitution used in PEG as the solutions typically diverges for "short" values of T_{go}. Figure 6.13 shows the flight path angle history, where the PEG profile deviations from the optimal solution are due to the non-optimal analytic solutions, which used polynomial approximations for the steering profiles.

It is interesting to note that the predicted jettison time from the PEG routine becomes fairly unstable at the staging point, shown in Fig. 6.14, at approximately 337 s.

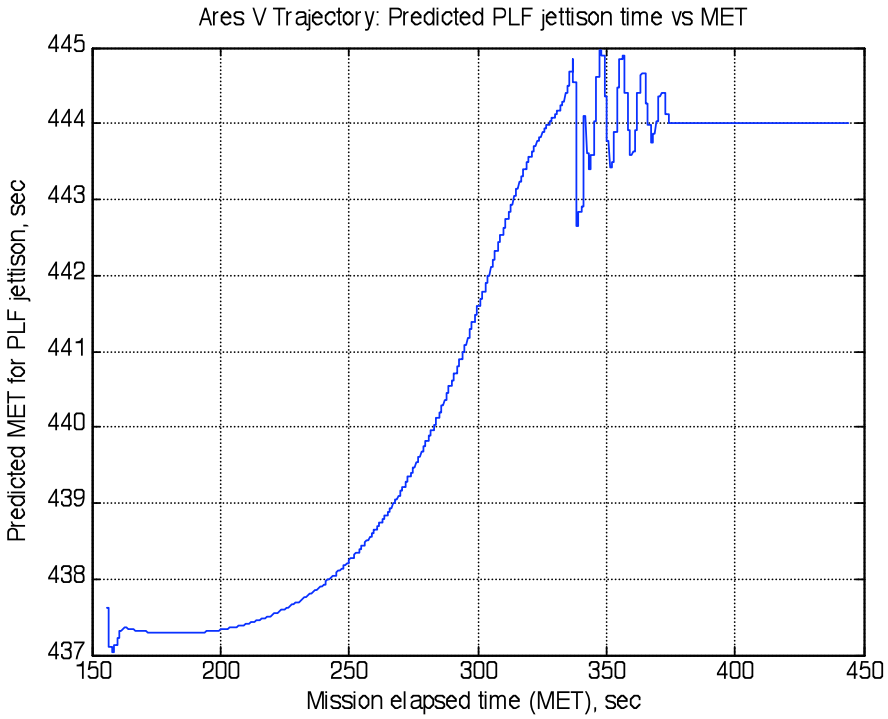

Figure 6.14: Predicted PLF jettison time vs. mission elapsed time.

The predicted MECO time, shown in Fig. 6.15, however, is very stable, and the mission elapsed time actually ends at the predicted MECO time of 771 s. The initial transient portion occurs for approximately the first ten passes to PEG, then stabilizes.

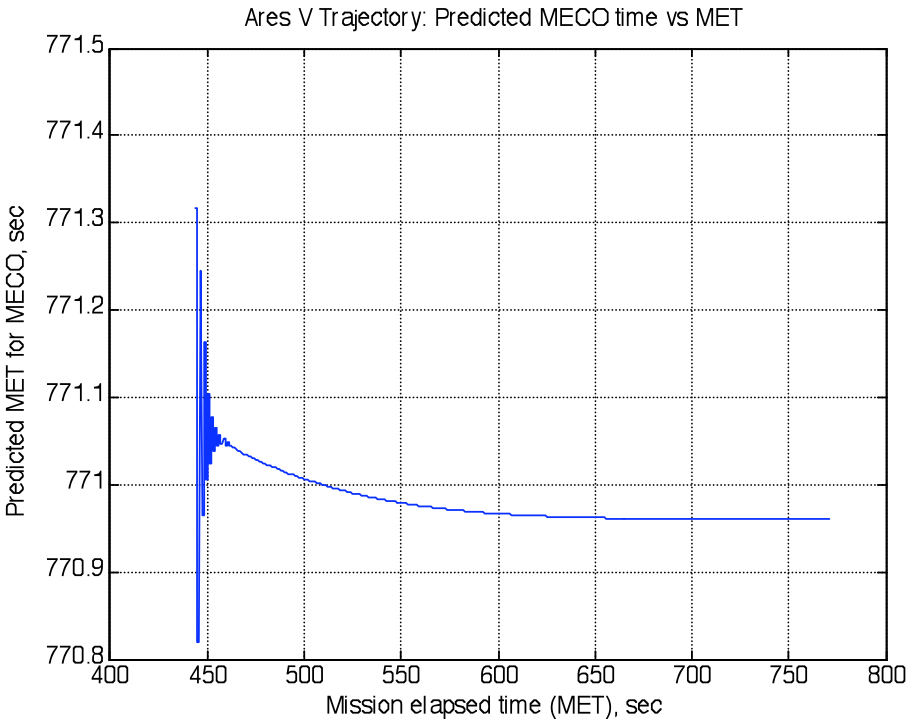

Figure 6.15: Predicted MECO time vs. mission elapsed time.

If the ascending node and angle of inclination histories resulting from the PEG solution are examined, the problems with steering, and thus, the deviation from the optimal solution, may be attributed. Figures 6.16 and 6.17 indicate that the respective angles are not only being constrained at the initial and final states, but also are being constrained at the staging point and the jettison event.

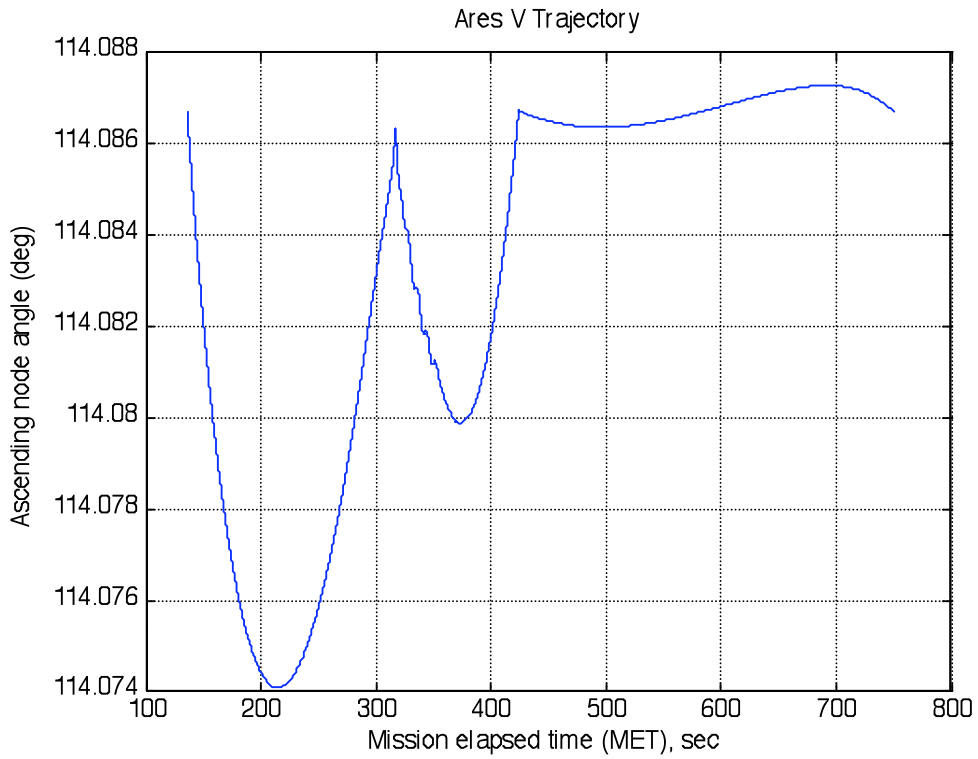

Figure 6.16: Profile of ascending node from PEG solution.

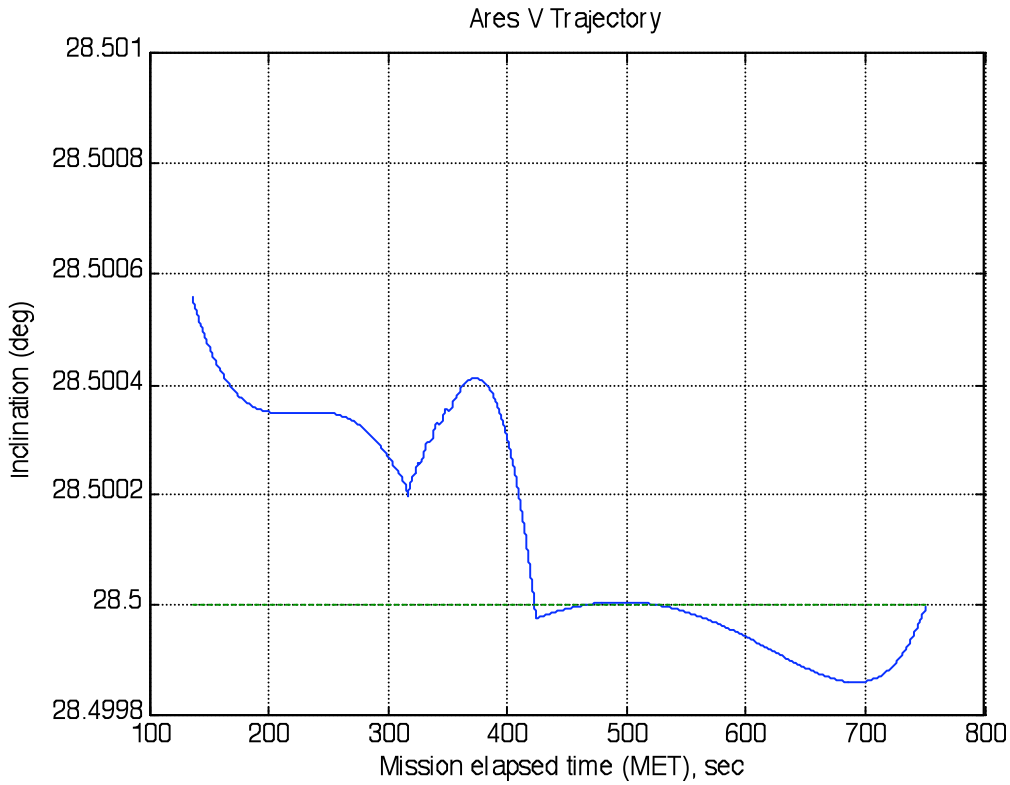

Figure 6.17: Profile of angle of inclination from PEG solution.

These additional constraints, which are not imposed in the optimal solutions, may be the cause of unnecessary out-of-plane steering, which would result in the unstable pitch profile and the longer flight times. Further testing could be done to eliminate these extra constraints and to verify whether the PEG solution would then match the optimal off-line ascent solution.

Perhaps another explanation for the poor PEG convergence of the ascent solution from start to PLF is the use of Jaggers' PEG formulation [23]. The complicated routine, formulated for the upper stage of the Shuttle, may not be able to handle the interior-point constraint discussed in this thesis. This would explain why the PEG simulation exhibits more optimal performance from PLF jettison to MECO conditions. Therefore, future work would include reformulating the PEG routine to determine how to release the extra constraints on steering at the staging points and to properly incorporate the interior state constraint for the first stage of the ascent trajectory.

Chapter 7

Conclusions

7.1 Summary and Conclusions

The vacuum ascent trajectory for the Ares V CaLV is solved using optimal control theory with interior-state constraints. Under the assumption of linear steering, the full costates were simplified and a method of direct parameter optimization was applied to find the optimal control steering parameters. Comparisons to the OTIS trajectory, provided by the Marshall Space Flight Center Trajectory and Performance Team, show similar trends in the trajectory parameters, despite simplifications in atmospheric and vehicle modeling made in the optimization routine.

The analytic solutions were also shown to successfully converge to the optimized trajectory. Though the inherent polynomial approximations caused slight differences in the optimal solutions, because the overall goal was to provide the on-line guidance simulation with an appropriate initial estimate, these differences were deemed negligible. Utilizing the analytic solutions as the initialization, the PEG simulation successfully converged to target conditions. The PEG solution also showed good comparison to the off-line optimization solution, and especially performed well during the second thrust stage from PLF jettison to the MECO conditions. Without the analytic solutions, PEG could not converge, which implies that the analytic solution may provide an alternate method in determining a good initial estimate for PEG to start its algorithm.

7.2 Future Work

Although this thesis presents the feasibility of using optimal control theory, direct optimization, and analytical methods to solve the ascent trajectory problem, there still remains a significant amount of work. First, the proper transformation, which would transform the linear steering parameters into the full costates, needs to be formulated, so that the analytic costate jump condition may be included in the optimization routine. It is desirable to take advantage of the analytic solution, as it decreases the number of parameters needed for optimization. Additional work should also be done by reformulating the PEG simulation, where the unnecessary constraints may be causing the solution to deviate from the optimal off-line solution.

To further validate the optimization routine, Monte Carlo simulations should be performed, which should include dispersions in the initial state vector and atmospheric characteristics. The simulations for this thesis used a fairly simple method of modeling atmospheric characteristics. A more complex, realistic method of modeling the atmospheric characteristics should be applied to the optimization routine in order to verify its robustness.

Appendix A

Exoatmospheric Powered Flight Guidance and Trajectory Optimization

A.1 Powered Explicit Guidance

The solution to the two-point boundary-value problem for exoatmospheric guidance and trajectory optimization considers all necessary conditions for optimality. A brief summary of the PEG method will be presented here, but full details are discussed in Ref. 21.

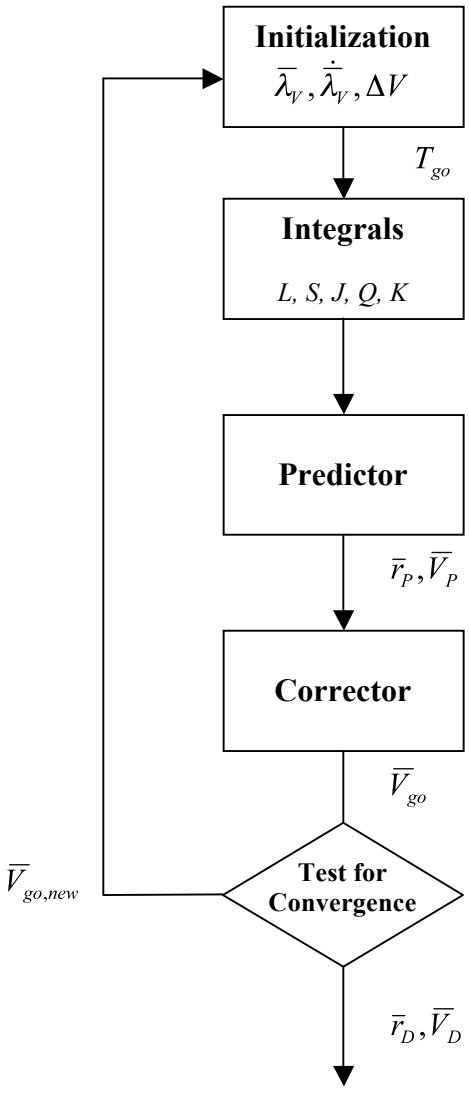

Figure A.1: Basic PEG routine schematic.

The iterative PEG algorithm, described by the basic schematic in Fig. A.1, self-starts with an arbitrary initial value $\dot{\bar{\lambda}}_V = 10^{-5}$, sets $\bar{\lambda}_V$ as a unit vector aligned with the velocity vector, and uses the impulsive solution for the initial ΔV. Then PEG computes the basic first order integrals, *L, S, J, Q, K*, and the Predictor step projects a trajectory to determine the predicted states, $\bar{r}_P$ and $\bar{V}_P$. The Corrector step makes the proper adjustments to determine the velocity-to-go, $\bar{V}_{go}$. A convergence test is performed to determine whether the desired velocity has been met, and is either returned to the vehicle's guidance scheme, or goes back to the initialization step.

References

[1] Anon., "The Space Launch Initiative: Technology to Pioneer the Space Frontier," NASA Marshall Space Flight Center, Pub 9-1250, FS 2001-06-122-MSFC, June, 2001.

[2] Best, J., Chavers, G., Richardson, L., and Cruzen, C., "Operational Concept for the NASA Constellation Program's Ares I Crew Launch Vehicle," AIAA Paper 2008-3562, SpaceOps Conference, Heidelberg, Germany, May 2008.

[3] Strong, E., Thomas, R., Vigil, A., and Cox, R., "Development of a Test & Verification Approach for the Constellation Program," AIAA Paper 2008-1625, U.S. Air Force TandE Days, Los Angeles, CA, Feb 2008.

[4] Martin, D.T., Sievers, R.F., O'Brian, R.M., and Rice, A.F., "Saturn V Guidance, Navigation, and Targeting," *Journal of Spacecraft and Rockets*, Vol.4, pp. 891-898, July 1967.

[5] McHenry, R.L., Brand T.J., Long, A.D., Cockrell, B.F., and Thibodeau III, J.R., "Space Shuttle Ascent Guidance, Navigation, and Control," *Journal of the Astronautical Sciences*, Vol. XXVII, No. 1, pp. 1-38, January-March, 1979.

[6] "Ascent Second Stage," *Ascent Guidance, Navigation, and Flight Control Workbook*, Lydon B. Johnson Space Center, Houston, Texas, 1979.

[7] Hanson, J.M., "A Plan for Advanced Guidance and Control Technology for 2nd Generation Reusable Launch Vehicles," AIAA Paper 2002-4557, Guidance, Navigation, and Control Conference, Monterey, CA, Aug 2002.

[8] Hanson, J.M., "Advanced Guidance and Control Methods for Reusable Launch Vehicles: Test Results," AIAA Paper 2002 4561, Guidance, Navigation, and Control Conference, Monterey, CA, Aug 2002.

[9] Dukeman, G., "Atmospheric Ascent Guidance for Rocket-Powered Launch Vehicles," AIAA Paper 2002-4559, Guidance, Navigation, and Control Conference, Monterey, CA, Aug 2002.

[10] Lu, P., Sun, H., and Bruce, T., " Closed-Loop Endo-Atmospheric Ascent Guidance," AIAA Paper 2002-4558, Guidance, Navigation, and Control Conference, Monterey, CA, Aug 2002.

[11] Lu, P., Griffin, B., Dukeman, G., Chavez, F., "Rapid Optimal Multi-Burn Ascent Planning and Guidance," AIAA Paper 2007-6773, Guidance, Navigation, and Control Conference, Hilton Head, SC, Aug 2007.

[12] Calise, A.J., Melamed, N., and Lee, S., "Design and Evaluation of a Three Dimensional Optimal Ascent Guidance Algorithm," *Journal of Guidance, Control, and Dynamics*, Vol. 21, No. 6, pp. 867-875, 1998.

[13] Gottlieb, R., Fowler, W., " Improved Secant Method Applied to Boost Trajectory Optimization," *Journal of Spacecraft and Rockets*, Vol. 14, No. 2, pp. 96-101, Feb 1977.

[14] Brusch, R., "Trajectory Optimization of the Atlas/Centaur Launch Vehicle," *Journal of Spacecraft and Rockets*, Vol. 14, No. 9, pp. 550-555, Sept 1977.

[15] Dux, I., Pinson, R., "Trajectory and Performance Team Summary: OTIS Revisions," Ares V VIPA Study Continuation, Jan 2007.

[16] Burrows, R.R., McDaniel, G.A., "A Method of Trajectory Analysis with Multi Mission Capability and Guidance Application," AIAA Paper No. 68-844, August 1968.

[17] Bryson, A.E., and Ho, Y.C., *Applied Optimal Control*, Hemisphere, Washington, D.C., pp. 42-87, 1975.

[18] Lawden, D.F., *Optimal Trajectories for Space Navigation*, Butterworth, London, UK, pp. 54-68, 1963.

[19] McAdoo, S.F., Jezewski, D.J., and Dawkins, G.S., "Development of a Method for Optimal Maneuver Analysis of Complex Space Missions," NASA TN D 7882, April, 1975.

[20] Kern, E.A., "Minimum-Fuel Thrust-Limited Transfer Trajectories Between Coplanar Elliptic Orbits," Ph.D. Thesis, Univ. of Michigan, Ann Arbor, Mich., 1968.

[21] Robbins, H.M., "An Analytical Study of the Impulsive Approximation," *AIAA Journal*, Vol. 4, No. 8, pp. 1417-1423, Aug 1966.

[22] Tarbet, D., "Optimum Continuous Control by a Method of Parameterization," Ph.D. thesis, Univ. of Houston, also TM X-58076, NASA, 1971.

[23] Jaggers, R.F., "An Explicit Solution to the Exoatmospheric Powered Flight Guidance and Trajectory Optimization Problem for Rocket Propelled Vehicles," AIAA Paper 77-1051, pp 566-578, 1977.